

AD-A069 209

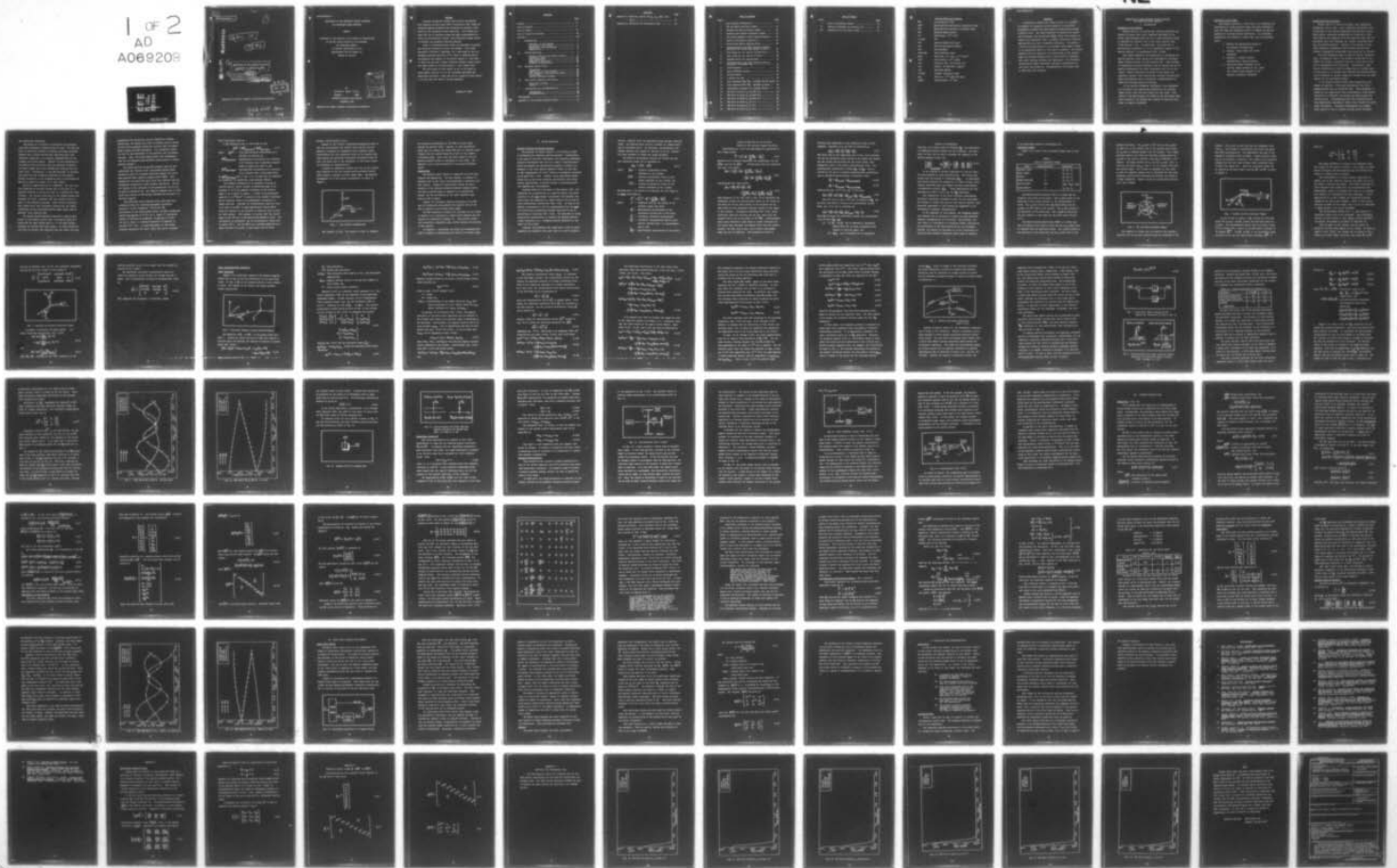
AIR FORCE INST OF TECH WRIGHT-PATTERSON AFB OHIO SCH--ETC F/G 17/7
ESTIMATION OF THE ANOMALOUS GRAVITY GRADIENT VIA PRECISION ANGL--ETC(U)
DEC 78 R W SMART

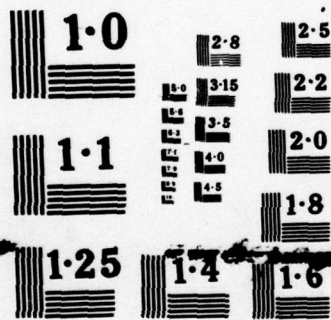
UNCLASSIFIED

AFIT/GGC/EE/79-3

NL

1 of 2
AD
A069209





NATIONAL BUREAU OF STANDARDS
MICROCOPY RESOLUTION TEST CHART

14

AFIT/GGC/EE/79-3

1

AD A069209

11 Dec 78

12 98 p.

DDC FILE COPY.

6 ESTIMATION OF THE ANOMALOUS GRAVITY GRADIENT VIA PRECISION ANGLE TRACKING.

9 Master's THESIS,

AFIT/GGC/EE/79-3 10 Wayne Richard Smart captain USAF

DDC RECEIVED JUN 1 1979 A

Approved for public release; distribution unlimited

012 225 Gu
79 05 29 126

AFIT/GGC/EE/79-3

ESTIMATION OF THE ANOMALOUS GRAVITY GRADIENT
VIA PRECISION ANGLE TRACKING

THESIS

Presented to the Faculty of the School of Engineering
of the Air Force Institute of Technology
Air Training Command
in Partial Fulfillment of the
Requirements for the Degree of
Master of Science

by

Richard W. Smart, B.E.E.

Captain USAF

Graduate Guidance and Control

December 1978

ADMISSION NO.	
RTM	Write Section <input checked="" type="checkbox"/>
ERC	Part Section <input type="checkbox"/>
UNCLASSIFIED	<input type="checkbox"/>
WARRANTY	
BY	
PERMISSION/AVAILABILITY CODES	
Dist.	AVAIL. and/or SPECIAL
A	

Approved for public release; distribution unlimited.

Preface

Inertial navigation systems and inertial instruments have improved so much since their introduction that today the unmodeled gravity anomalies are becoming the dominant error source in the navigation error equations. This thesis proposes the use of precision range and angle measurements between two accelerometer triads and an Extended Kalman Filter to estimate the anomalous gravity gradient.

Prior to undertaking this study, my knowledge of geodesy and nonlinear estimation theory was minimal. This study presented a difficult challenge, but I was aided by the outstanding teaching abilities of Dr. Peter S. Maybeck and by the guidance and support of my advisor Captain J. Gary Reid. To these two men and to Major Salvatore Balsamo, whose advice and humor helped at critical points, I owe a great debt.

The true value of this thesis is not to be found in these pages, however, but in the increased knowledge and analytical abilities I take with me as a result of this effort. It is this last for which I am most grateful.

Richard W. Smart

Contents

	Page
Preface	ii
List of Figures	v
List of Tables	vi
List of Terms and Acronyms	vii
Abstract	viii
I. Introduction	1
Statement of the Problem	1
Objectives of the Study	2
Assumptions and Limitations	3
Organization	8
II. System Modelling	9
Concept Overview and Chapter Outline	9
Coordinate Frames	14
State Equations	20
Measurement Equations	36
Hardware Configurations	37
III. Extended Kalman Filter	43
Formulation	43
Application to this Problem	46
U-D Covariance Factorization Update	54
Truth Model	58
Gravity Gradient Estimate	59
IV. Monte Carlo Analysis and Results	63
Monte Carlo Method	63
Results	65
V. Conclusions and Recommendations	69
Conclusions	69
Recommendations	69
Bibliography	72
Appendix A: The Gravity Gradient Tensor	75

Contents

	Page
Appendix B: Numerical Values for \underline{x}_0 , \underline{P}_0 , $\underline{Q}(t)$, and $R(t_i)$	77
Appendix C: PSD Plots for Disturbance Data	79

List of Figures

Figure		Page
1	Full System Configuration	7
2	ECI and ECEF Coordinate Frames	15
3	Tracker and LOS Coordinate Frames	16
4	Inertial and Tracker Coordinate Frames	18
5	Free-Body Diagram of Basic System Elements ..	20
6	Gravity Disturbance Quantities	27
7	First-Order Markov Shaping Filter	29
8	Autocorrelation and Power Spectral Density Functions for First-Order Markov Process	29
9	True Delta G _x , G _y , and G _z (10,000 feet)	33
10	True Delta G _x , G _y , and G _z (0 feet)	34
11	Shaping Filter for Random Bias	35
12	Autocorrelation and Power Spectral Density Functions for Random Bias	36
13	Interferometer	38
14	Basic STARTRAC Concept	40
15	Autocollimator	41
16	F Matrix for EKF	51
17	True Gradients Γ_{xx} , Γ_{xy} , and Γ_{xz} (10,000 feet)	61
18	True Gradients Γ_{xx} , Γ_{xy} , and Γ_{xz} (0 feet) ...	62
19	Performance Analysis of a Kalman Filter	63
20	PSD Plot of Delta G _x (10,000 ft.)	80
21	PSD Plot of Delta G _y (10,000 ft.)	81
22	PSD Plot of Delta G _z (10,000 ft.)	82
23	PSD Plot of Delta G _x (0 ft.)	83
24	PSD Plot of Delta G _y (0 ft.)	84
25	PSD Plot of Delta G _z (0 ft.)	85

List of Tables

Table		Page
I	List of Coordinate Frames	14
II	Gravity Variations for Western U.S.	30
III	Operations for One Filter Cycle	57

List of Terms and Acronyms

$\widehat{\text{sec}}$	an arcsecond, $1^{\circ}/60$
ECEF	<u>E</u> arth- <u>C</u> entered <u>E</u> arth- <u>F</u> ixed coordinate frame
ECI	<u>E</u> arth- <u>C</u> entered <u>I</u> nertial coordinate frame
EKF	<u>E</u> xtended <u>K</u> alman <u>F</u> ilter
EU	<u>E</u> ötvös <u>U</u> nit, 10^{-9} sec^{-2}
i-frame	ECI
IMU	<u>I</u> nertial <u>M</u> easurement <u>U</u> nit
INS	<u>I</u> nertial <u>N</u> avigation <u>S</u> ystem
LOS	<u>L</u> ine- <u>o</u> f- <u>S</u> ight
LOS-frame	LOS coordinate frame
mgal	Milli-gal, $10^{-3} \text{ gal} = 10^{-5} \text{ m/sec}^2$
mrad	Milli-radian, 10^{-3} radian
nmi	Nautical mile, 1852 meters (m)
rad	Radian, $57.2957795131 \text{ degrees}$
rms	<u>R</u> oot <u>M</u> ean <u>S</u> quare
T-frame	Tracker coordinate frame
μg	Micro-g , $10^{-6} \text{ g} \approx 0.981 \text{ mgal}$
μrad	Micro-radian, 10^{-6} rad

Abstract

A preliminary feasibility study was done on a proposal to estimate the anomalous gravity gradient via precision measurements between two accelerometer triads moving through a gravity field. The state equations to describe the system were developed, and an Extended Kalman Filter was designed to exploit the measurement data. A simple, first-order numerical approximation was used in gradient estimation. In addition, a brief conceptualization of the hardware which might be used in an operational system of this type is included. The results indicate that the numerical ill-conditioning in the problem makes the Extended Kalman Filter a poor choice of estimator. Even after scaling variables and employing a U-D Covariance factorization update algorithm, numerical instabilities in the filter were observed. Recommendations for further work on this topic are included.

ESTIMATION OF THE ANOMALOUS GRAVITY GRADIENT VIA PRECISION ANGLE TRACKING

I. Introduction

Statement of the Problem

State-of-the-art in terrestrial inertial navigation has reached the point where one's imperfect knowledge of the earth's gravitational field (G , due to mass attraction alone) is assuming the dominant role in the error equation (Ref. 17:269 and Ref. 4:2). In particular, INS errors due to gravitational anomalies, or to the unmodelled changes in the gravity gradient, are predominant (Ref. 17:269).

This thesis addresses the feasibility of estimating the gravity gradient using, among other measurements, precision angle tracking between two high accuracy IMU. Other methods of estimating the gravity gradient such as through the use of gravity gradiometers now under development will not be discussed. Should feasibility be shown in this study, the potential benefits could include more accurate inertial navigation performance and an alternative to gradiometers for rapid and wide-area gravity surveying.

Of the several estimation techniques in use throughout the scientific and engineering communities, the Extended Kalman filter (EKF) has been chosen for this study. This choice of the EKF estimator was based on the non-linear dynamics involved in the problem and a desire to keep the estimator as simple as possible.

Objectives of the Study

The primary objective of this study is to determine the feasibility of using precision range and angle tracking between two IMUs and employing an EKF to estimate the gravity gradient in a moving vehicle environment. To investigate feasibility, the problem is broken down into the following parts:

1. Develop the hypothetical design of the hardware configuration.
2. Develop a truth model and an EKF estimator.
3. Generate a "flight" profile representing a typical mission.
4. Using the models developed in (2) and the flight profiles of (3), carry out a Monte Carlo analysis of the gradient estimation technique.

Assumptions and Limitations

Because this is a feasibility study, many simplifying assumptions will be made. Also, optimistic performance characteristics of the various measurement devices will be used. These simple, optimistic assumptions are justified in that they simplify the analysis and at the same time they test the hypothesis that this technique can, indeed, accurately estimate the gravity gradient. Failure of the process to work under optimistic assumptions would clearly indicate that further investigation along these lines would not be fruitful.

The first assumption made is that the vehicle (aircraft, ship, or submarine) used in the gradient survey will be operated in a benign environment (calm air or sea) and it will not be undergoing violent maneuvers. Nevertheless, there will be vibration and vehicle bending modes to contend with. In this study it is assumed that vibration and bending effects can be minimized by careful design and construction, and these effects are not considered further.

In the flight profiles tested only straight and level flight is simulated. This would typically be true for a mapping mission such as envisioned here. This assumption is really not too restrictive since accelerometers (here assumed sensitive to 10^{-8} m/sec²) can measure and hence account for vehicle motion. Accelerometers with this sensitivity have been demonstrated according to Slater (Ref. 24:198) for earth-based instruments. Instrument misalignments are assumed known a priori or can be obtained through proper alignment

and calibration techniques.

The system to be studied is non-linear and therefore non-linear estimation techniques must be used. The EKF used here, as with most methods of treating non-linear problems, assumes that a linear system model operating about some reference trajectory is an adequate representation of the original non-linear system. Implicit in this assumption is the premise that deviations from the reference trajectory are small enough that linear methods for treating them are still valid. Furthermore, in the EKF the model is relinearized about the new estimated trajectory at each update. Further discussion on the assumptions made in developing the EKF can be found in Chapter III of this report.

Only two flight profiles are simulated. The first profile simulates an aircraft flying west at 100 mi/hr at a constant altitude of 10,000 feet and at a constant 35° north latitude. The initial conditions for the flight profile are latitude 35° north, longitude 239° east measured with respect to the Greenwich meridian. These initial conditions were chosen since they correspond closely with the center coordinates of the point-mass gravity model region used to generate "true" gravity data.

The second profile generated simulates a ship or submarine at the surface of the ocean traveling due west at 6 knots with the same initial point as in the first profile. Although the initial point and, indeed, the whole profile is over land in reality, the identical path was chosen for both

simulations for convenience and for comparative reasons. Intuitively, the slower and lower in altitude profile should provide better gradient estimation accuracy than the higher speed, higher altitude simulation. One fundamental reason for this is the attenuation of the gradient with increasing altitude. Also, the slower speed allows more integration time for the anomalous gravitational accelerations to affect position changes.

The actual gravity and gravity gradient data for the truth model was obtained from a point-mass gravity model included as part of a general spherical harmonic and point-mass gravity model computer program called GTGRV. This program and its associated data files were obtained from the Geodynamics Corporation, Santa Barbara, California. Pertinent details of the structure of the program and its use can be found in Reference 20. All computer programs used in this study were written in CDC Fortran Extended and executed on a CDC 6600 computer.

The point-mass model included seven point-mass sets contained within the following geographic boundaries:
latitude = 12.5° N; longitude = 207.5° - 272.5° E.
Distribution of the point-masses within the above boundaries varied from spacing of 5° for set 1, where ($^{\circ}$) represents degrees of latitude or longitude, to spacing of $0.3125'$ for set 7, where ($'$) represents minutes of longitude or latitude ($1^{\circ} = 60'$). A point-mass model of this detail probably represents the "best" model that can be obtained

from unclassified sources.

A key assumption made in this study is that

$$g(r) = g(r)_{\text{spherical harmonics}} + g(r)_{\text{point masses}} \quad (1-1)$$

where, $g(r)$ = total gravitational acceleration as a function of position, r ,

$g(r)_{\text{spherical harmonics}}$ = gravitational acceleration as a function of r obtained from a spherical harmonic model of degree and order 8, and

$g(r)_{\text{point masses}}$ = gravitational acceleration as a function of r obtained from a point-mass model.

The $g(r)_{\text{point masses}}$ term in eqn. (1-1) is used here to represent the anomalous, or unmodelled, gravitational effects.

The hardware configuration is assumed to include an electro-optical tracker capable of measuring range to an accuracy of 10^{-5} m and angular deviations of the line-of-sight to an accuracy of $1 \mu\text{rad}$. A triad of accelerometers sensitive to 10^{-8} m/sec² is mounted at the tracker's position, and an identical triad of accelerometers is mounted on a target platform. Although the accelerometers would not have to be part of an IMU, in many applications several IMU's would be available in the aircraft or ship and could be used for this purpose. This assumes, of course, that the instruments in the IMU are of the sensitivity mentioned above. For convenience in discussion, the two accelerometer triads will be called IMU's. The two IMU's are initially separated by a known distance (10 meters in this study) and are flown

through a known gravity field.

Another of the critical simplifying assumptions made is that all accelerometer and tracker noise sources can adequately be modelled as independent white Gaussian noises. Justification for this assumption rests on the premise that very precise and accurately calibrated instruments would be used, and hence most of the systematic or bias errors would be calibrated or compensated for.

A system to completely estimate all five of the independent elements of the nine element gravity gradient matrix would require a minimum of three target IMUs. One possible arrangement for a full system configuration is shown in Figure 1.

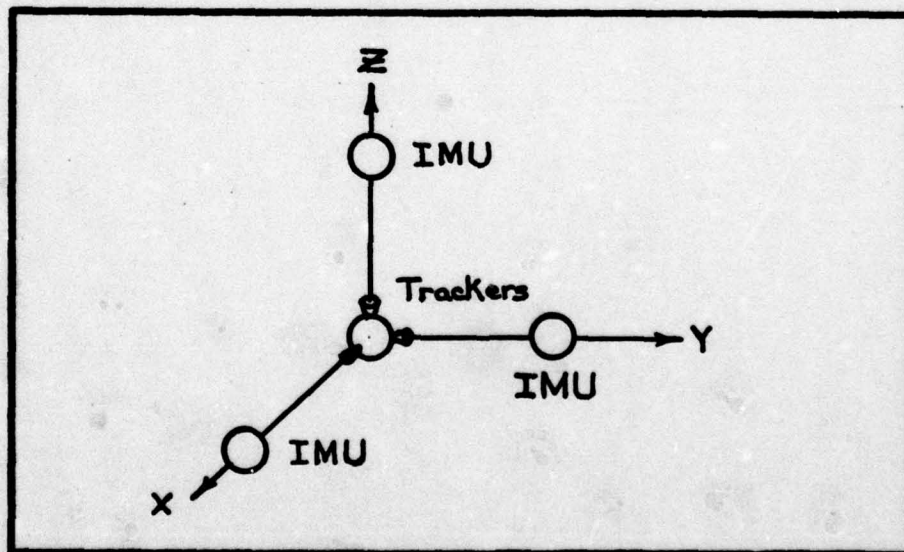


Fig. 1 Full System Configuration

The trackers in Fig. 1 are needed in order to estimate

the relative accelerations of the IMU's as they travel through the gravity field. However, in this feasibility study only one tracker and target IMU pair is included, specifically the one located along the X-axis of the tracker coordinate frame. Thus, only the first column of the 3×3 gravity gradient matrix is estimated in this study. See appendix A for a brief discussion of the gravity gradient tensor.

Organization

The material which follows is organized into five main chapters and appendices. The next chapter, or Chapter II, presents most of the theory and establishes a foundation for what follows. Chapter II specifically covers the basic elements of the proposed anomalous gradient mapping system, how these elements might be employed in an operational system, and the derivations of the state equations upon which an EKF is based.

Chapter III includes a general discussion of the EKF and its formulation and presents the specific form of the EKF as applied to the problem under study.

The EKF discussed in Chapter III and based on the theory in Chapter II is subjected to a Monte Carlo analysis and the results are discussed in Chapter IV. This section covers test objectives, simulation data, filter tuning, and accuracy of the results.

In Chapter V, conclusions are drawn and recommendations made in regards to applications and topics for further study.

II. System Modelling

Concept Overview and Chapter Outline

The problem, as stated earlier, is to develop a means of estimating the anomalous gravity gradient. Gradiometers, a new class of inertial instruments, are presently undergoing extensive development and test by a number of manufacturers. These instruments are specifically designed to measure the elements of the total gravity gradient tensor in real-time so that compensation for their effects on navigation estimates can be made (Ref. 4:34). However, since operational gradiometers are no near-term certainty, particularly for moving vehicle applications, alternate methods of performing gradient mapping bear investigation.

Although Einstein's Principle of Equivalence (Ref. 2:2) eliminates the accelerometer as a gravity sensor, two accelerometers in the same dynamic environment with parallel sensitive axes and separated by a small distance can be used to sense differential acceleration (Ref. 4:36). As long as the dynamic environments of the two accelerometers are the same, the differential acceleration between them must be due to gravitational variations (Ref. 4:36). The principle of using differential accelerations to estimate the spatial gravitational variations (i.e., anomalous gravity gradient) is the basis for this study.

Consider two platforms each supporting a triad of accelerometers and separated from each other by a short distance.

Further, consider these two platforms moving through a gravity field. One platform also carries a tracker for reasons which will be discussed later. The platform, accelerometers, and tracker together will simply be referred to as the "tracker." The other platform is termed the target platform.

The relative acceleration between the tracker and target coordinate frames can be expressed as

$$\underline{a}_{rel}^i = P_i^2 \underline{a}_b - P_i^2 \underline{a}_T \quad (2-1)$$

where, \underline{a}_{rel}^i = relative acceleration vector
expressed in the i-frame,

$P_i^2 \underline{a}_b$ = inertial acceleration vector at the
target expressed in the i-frame, and

$P_i^2 \underline{a}_T$ = inertial acceleration vector at the
tracker expressed in the i-frame.

Britting (Ref. 2:32) gives as an equation for the output of an ideal accelerometer,

$$\underline{f}^a = \underline{C}_i^a \ddot{r}^i - \underline{G}^a + \sum_{K'} [\underline{G}_K - \underline{G}_{K'}^a] \quad (2-2)$$

where: K' = summation over all the bodies of the
universe except the earth,

\underline{G}^a = gravitational acceleration at the
instrument location due to the earth,

\ddot{r}^i = inertially referenced acceleration,

\underline{C}_i^a = coordinate transformation matrix relating the inertial axes i to accelerometer axes a, and

$\underline{G}_{K'}$ = gravitational acceleration at the earth's

center of mass due to all of the k
bodies in the universe except the earth.

Rearranging eqn. (2-2) and expressing all quantities in
the i-frame yields

$$\ddot{\underline{r}}^i = \underline{f}^i + \underline{G}^i - \sum_{K'} [\ddot{\underline{G}}_{K'}^i - \underline{G}_{K'}^a] \quad (2-3)$$

Equation (2-3) actually represents two expressions, one for
 $\rho_1^2 \underline{r}_b$ and one for $\rho_1^2 \underline{r}_T$. Substituting these two equations
into eqn. (2-1) gives

$$\underline{a}_{rel}^i = \left\{ \underline{f}_b^i + \underline{G}_b^i - \sum_{K'} [\ddot{\underline{G}}_{K_b}^i - \underline{G}_{K_b}^i] \right. \\ \left. - \left\{ \underline{f}_T^i + \underline{G}_T^i - \sum_{K'} [\ddot{\underline{G}}_{K_T}^i - \underline{G}_{K_T}^i] \right\} \right\} \quad (2-4)$$

and grouping like terms yields,

$$\underline{a}_{rel}^i = (\underline{f}_b^i - \underline{f}_T^i) + (\underline{G}_b^i - \underline{G}_T^i) \\ - \left\{ \sum_{K'} [\ddot{\underline{G}}_{K_b}^i - \underline{G}_{K_b}^i] - \sum_{K'} [\ddot{\underline{G}}_{K_T}^i - \underline{G}_{K_T}^i] \right\} \quad (2-5)$$

Each component of the last term in eqn. (2-5) represents the
difference between the gravitational effect at the center of
the earth due to all other bodies in the universe and the
same effect at the instrument location (either at the target
or the tracker). According to Britting (Ref. 2:32), these
difference terms for the moon and the sun, which have the
largest effect, are on the order of $10^{-7} |G|$. Heuristically,
since these difference terms would be nearly identical for
two bodies only 10m apart (as assumed here) near the earth's
surface, the last term in eqn. (2-5) becomes vanishingly
small and can be neglected. This assumption should be

verified more rigorously in any subsequent study of this proposal. Equation (2-5) can then be rewritten as

$$\underline{a}_{rel}^i = (\underline{f}_b^i - \underline{f}_T^i) + (\underline{G}_b^i - \underline{G}_T^i) \quad (2-6)$$

The first term on the right-hand side of eqn. (2-6) accounts for all the non-field forces acting on the target and tracker and the second term accounts for the field forces, here assumed due only to the earth's gravitational field. The gravitational acceleration vectors, \underline{G}_b and \underline{G}_T , can be written as the sum of a modelled gravitational acceleration and an unmodelled gravitational acceleration, thus,

$$\underline{G}_b^i = \underline{g}_{b(model)}^i + \underline{g}_{b(unmodelled)}^i \quad (2-7a)$$

$$\underline{G}_T^i = \underline{g}_{T(model)}^i + \underline{g}_{T(unmodelled)}^i \quad (2-7b)$$

Substituting eqn. (2-7) into eqn. (2-6) gives

$$\underline{a}_{rel}^i = (\underline{f}_b^i - \underline{f}_T^i) + (\underline{g}_b^i - \underline{g}_T^i)_{model} + (\underline{g}_b^i - \underline{g}_T^i)_{unmodelled} \quad (2-8)$$

The last term in eqn. (2-8) can be replaced by $\delta \underline{g}$ and an error term added to account for accelerometer errors.

Thus, eqn. (2-8) can be rewritten as

$$\underline{a}_{rel}^i = (\underline{f}_b^i - \underline{f}_T^i) + (\underline{g}_b^i - \underline{g}_T^i)_{model} + \delta \underline{g} + \underline{\epsilon} \quad (2-9)$$

where $\underline{\epsilon}$ represents the difference between the accelerometer error vectors $(\underline{\epsilon}_b - \underline{\epsilon}_T)$.

If, (1) \underline{f}_b and \underline{f}_T can be measured in coordinate frames which are of known orientation with respect to inertial space, and

(2) \underline{a}_{rel}^i can be estimated by an independent

source of information,

then eqn. (2-1) may be used to estimate, $\delta \underline{g}$, the difference in unmodelled gravity between the two locations. The estimate, in turn, can be used to estimate the elements of the gravity gradient tensor via

$$\left[\frac{\partial \underline{g}}{\partial \underline{r}} \right]_{\text{unmodelled}} \approx \left[\frac{\delta \hat{\underline{g}}}{\delta \underline{r}} \right] = \begin{bmatrix} \frac{\delta \hat{g}_x}{\delta r_x} & \frac{\delta \hat{g}_y}{\delta r_y} & \frac{\delta \hat{g}_z}{\delta r_z} \end{bmatrix} \quad (2-10)$$

It is critical to satisfy conditions (1) and (2) above for this proposal to work satisfactorily. This thesis addresses only the problem of estimating \underline{a}_{rel}^i . In particular, this thesis examines the capability of a line-of-sight (LOS) tracker producing range and angular deviation measurements to adequately estimate \underline{a}_{rel}^i . These measurements are then employed by an EKF to solve for the $\delta \underline{g}$ components.

Full examination of the first condition (maintaining precision orientation information about the two accelerometer triads) is beyond the scope of this thesis; however, some potential approaches to this problem are suggested in the discussion of hardware configurations.

In the remainder of this chapter, the foregoing estimation problem will be developed in detail and some potential hardware configurations are described. Specifically, the next topic is a discussion of coordinate frames, followed by the development of the state equations for the estimator. Finally, the chapter is concluded by a brief description of some potential hardware components which might be employed

in an operational system as envisioned here.

Coordinate Frames

Table I is a list of the coordinate frames used in this study.

Table I
List of Coordinate Frames

Frame	Sub/superscript	Components
Inertial (ECI)	i	x_i, y_i, z_i
Earth (ECEF)	e	x_e, y_e, z_e
Tracker	T	x_T, y_T, z_T
Target Platform	b	x_b, y_b, z_b
Line-of-sight	LOS	$x_{LOS}, y_{LOS}, z_{LOS}$
Accelerometer	a	x_a, y_a, z_a

The Earth-Centered-Inertial (ECI) or i-frame has its origin at the center of the earth. The x_i -axis points in the direction of the vernal equinox, or the constellation of Aries. The y_i -axis lies in the equatorial plane with the x_i -axis, but 90° east of the x_i -axis. The z_i -axis points in the direction of the north pole. The i-frame is non-rotating with respect to the stars and the earth turns relative to it.

The Earth-Centered Earth-Fixed (ECEF) or e-frame also has its origin at the earth's center and the x_e - y_e plane also is coplanar with the equatorial plane. The z_e -axis points in the direction of the north pole and the x_e -axis lies in the

Greenwich meridian. The y_e -axis is 90° east of the x_e -axis. At time $t=0$, or the initial time of the problem under study, the x_e -axis is assumed aligned with the x_i -axis. The e-frame has axes fixed in the earth and therefore rotates about the z_e -axis at the earth's rotation rate, $\omega_{ie} = 7.292115147 \times 10^{-5}$ rad/sec. The angle between the x_i and the x_e axes, then, is found by the product $\omega_{ie} t$, where t is the elapsed time since the problem began. The e-frame is important in this study in that the computer program used to calculate the true gravitational accelerations and gradients produces its values in e-frame components. Figure 2 shows the relationship between the e and i-frames.

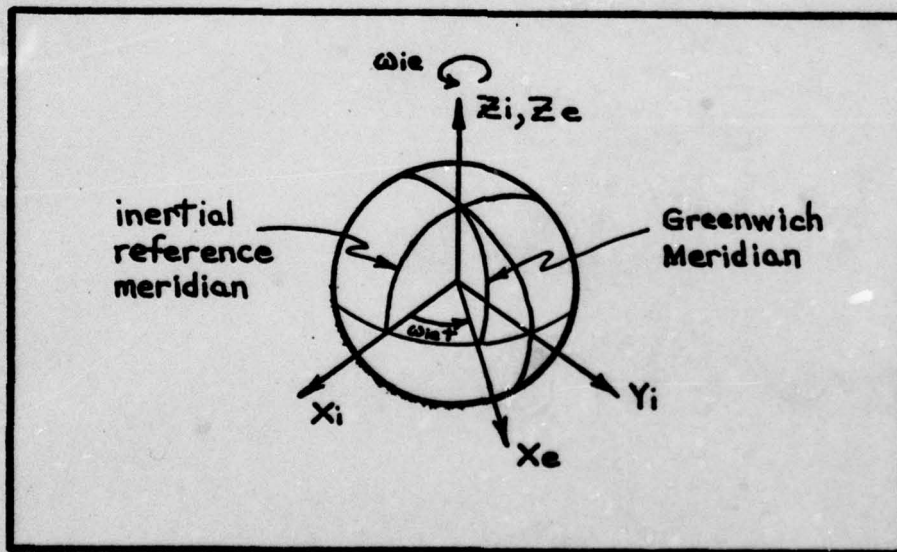


Fig. 2 ECI and ECEF Coordinate Frames

The tracker or T-frame has its origin at the tracker's location with the x_T -axis oriented along the boresight of the

tracker. The y_T and z_T axes then form an orthogonal triad with x_T . The T-frame is instrumented with three rate gyros and three accelerometers. The measurements are made in the tracker's coordinate frame (T-frame). Because perfect tracking is not possible in practice, the T-frame is not perfectly aligned with the true line-of-sight (LOS) coordinate frame in which the target lies. These two coordinate frames can be related by two Euler angle rotations $\delta\eta$ and $\delta\epsilon$ as shown in Figure 3.

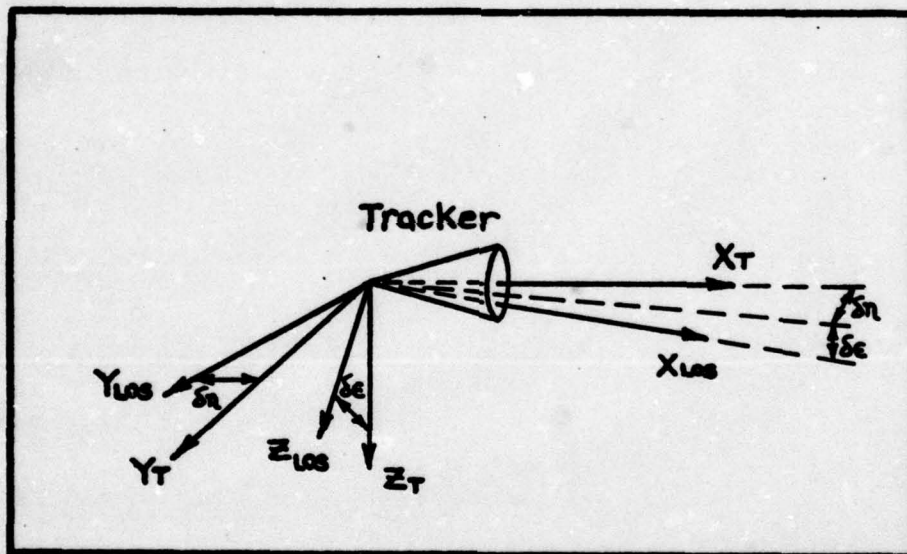


Fig. 3 Tracker and LOS Coordinate Frames

As can be seen in Figure 3, $\delta\eta$ rotates the LOS-frame about the z_T -axis, and $\delta\epsilon$ rotates the LOS-frame about the y_T -axis. The transformation matrix which will map a vector in the T-frame into a vector in the LOS-frame is denoted by the symbol C_T^{LOS} . For $\delta\eta$ and $\delta\epsilon$ in the microradian range, as would be the case for near-perfect tracking, C_T^{LOS} is

given by,

$$\underline{C}_T^{LOS} = \begin{bmatrix} 1 & \delta\eta & -\delta\epsilon \\ -\delta\eta & 1 & 0 \\ \delta\epsilon & 0 & 1 \end{bmatrix} \quad (2-11)$$

The target platform or b-frame is an orthogonal triad with origin at the target's location. The b-frame is instrumented with gyros and accelerometers and its attitude with respect to inertial space is known.

The accelerometer or a-frame actually represents two frames, one at the tracker's location (a_T -frame) and one at the target's location (a_b -frame). This frame represents the three sensitive axes along which the accelerometers make measurements, since it is assumed that there is no misalignment between the instruments and their mountings. In this application the a_b and b-frames are considered perfectly aligned as are the a_T and T-frames. Later in this section reference is made to the a-frame, and it is to be understood to apply equally to the a_b and a_T -frames.

The relationships between the i, e, and Tracker or T coordinate frames will now be developed. This development and much of what follows in this chapter closely parallels the similar development by Mitchell in Reference 18.

From the gyros on the tracker, one can obtain the tracker's attitude with respect to the i-frame. As shown in Figure 4 (Ref. 18:12), the T-frame can be related to the i-frame by two Euler angle rotations, here called Θ and ϕ .

As given by Mitchell (Ref. 18:13), the coordinate transformation matrix from the i-frame to the T-frame is

$$\underline{C}_i^T = \begin{bmatrix} \cos \theta \cos \phi & \sin \theta \cos \phi & -\sin \phi \\ -\sin \theta & \cos \theta & 0 \\ \cos \theta \sin \phi & \sin \theta \sin \phi & \cos \phi \end{bmatrix} \quad (2-12)$$

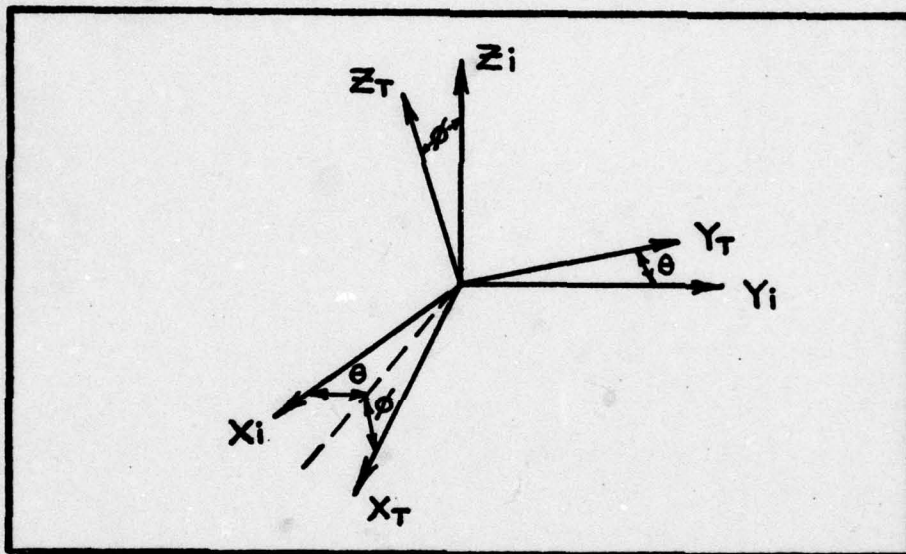


Fig. 4 Inertial and Tracker Coordinate Frames

It remains to determine the Euler angles and .
Again, borrowing from Mitchell (Ref. 18:14),

$$\begin{aligned} \theta &= \tan^{-1} \left(\frac{R_y}{R_x} \right), R_x > 0 \\ &= \tan^{-1} \left(\frac{R_y}{R_x} \right) + \pi, R_x < 0 \end{aligned} \quad (2-13)$$

and

$$\phi = \tan^{-1} \left[\frac{-R_z}{(R_x^2 + R_y^2)^{1/2}} \right] \quad (2-14)$$

where R_x , R_y , and R_z are the three components of the

relative position vector of the target from the tracker expressed in the i-frame.

One additional coordinate transformation matrix is needed to transform vectors between the e-frame and the i-frame. This transformation is given by Britting (Ref. 2:36) as,

$$\underline{C}_e^i = \begin{bmatrix} \cos \omega_{ie}t & -\sin \omega_{ie}t & 0 \\ \sin \omega_{ie}t & \cos \omega_{ie}t & 0 \\ 0 & 0 & 1 \end{bmatrix} \quad (2-15)$$

This completes the discussion of coordinate frames.

State and Measurement Equations

State Equations

Figure 5 is a free-body diagram of the gradient mapping system and is used to aid the derivations of the state equations. In Fig. 5, \underline{R} is the relative position vector between \mathbf{o} and \mathbf{b} , the origins of the tracker and target platform frames respectively.

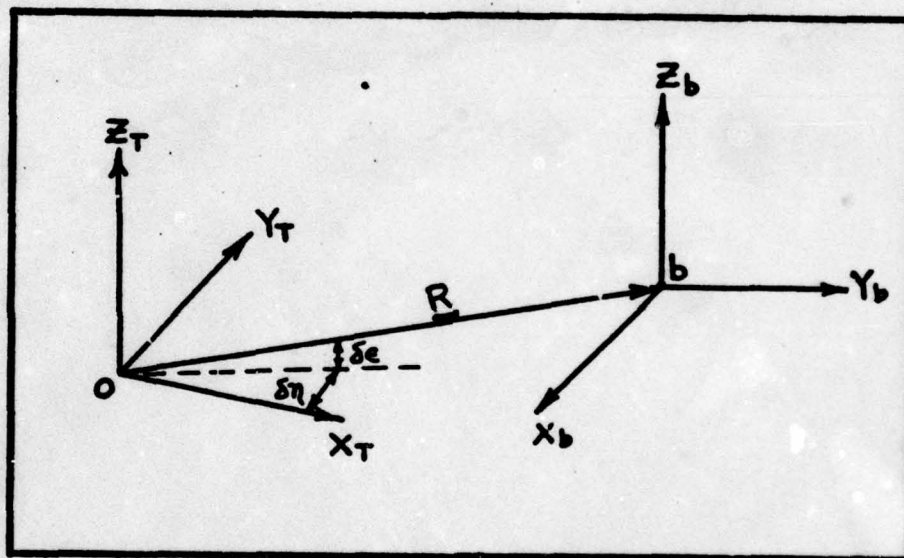


Fig. 5 Free-Body Diagram of Basic System Elements

The magnitude of \underline{R} , or $|\underline{R}|$, is the scalar range variable r . Taking the second derivative of \underline{R} with respect to inertial space and applying the Theorem of Coriolis as needed gives (Ref. 18:19),

$$\begin{aligned} \underline{P}_1^2 \underline{R} = \underline{P}_{LOS}^2 \underline{R} + 2 \underline{\omega}_{LOS} \times \underline{P}_{LOS} \underline{R} + \underline{P}_{LOS} \underline{\omega}_{LOS} \times \underline{R} \\ + \underline{\omega}_{LOS} \times (\underline{\omega}_{LOS} \times \underline{R}) \quad (2-16) \end{aligned}$$

\dot{p} = time derivative,

\dot{p}^2 = second time derivative,

\dot{p}_i, \dot{p}_{LOS} = time derivative with respect to the i and LOS-frames respectively,

ω_{LOS} = angular velocity vector of the LOS with respect to the i -frame, and

\times = vector cross product operation.

Equation (2-16) is a physical vector equation (i.e., the vector components of \underline{R} are not expressed in any particular coordinate frame). To make equation (2-16) a mathematical vector equation choose, say, the LOS coordinate frame to work in. Defining the term $\dot{p}_i^2 \underline{R}$ as \underline{a}_{rel} (the relative acceleration between points o and b of Fig. 5) and writing out the vectors in eqn. (2-16) in component form yields,

$$\begin{bmatrix} a_{relx} \\ a_{rely} \\ a_{relz} \end{bmatrix} = \begin{bmatrix} \dot{p}_{LOS}^2 r \\ 0 \\ 0 \end{bmatrix} + 2 \begin{bmatrix} 0 \\ \dot{p}_{LOS} r \omega_{LOSz} \\ -\dot{p}_{LOS} r \omega_{LOSy} \end{bmatrix} + \begin{bmatrix} 0 \\ r \dot{p}_{LOS} \omega_{LOSz} \\ -r \dot{p}_{LOS} \omega_{LOSy} \end{bmatrix} \quad (2-17)$$

$$+ \begin{bmatrix} -r(\omega_{LOSy}^2 + \omega_{LOSz}^2) \\ r \omega_{LOSx} \omega_{LOSy} \\ r \omega_{LOSx} \omega_{LOSz} \end{bmatrix}$$

Solving eqn. (2-17) for the derivative terms $\dot{p}_{LOS}^2 r$,

$\dot{p}_{LOS} \omega_{LOSz}$, and $\dot{p}_{LOS} \omega_{LOSy}$ yields the following three scalar equations:

$$\dot{p}_{LOS} r = a_{relx} + r(\omega_{LOSy}^2 + \omega_{LOSz}^2) \quad (2-18)$$

$$P_{LOS} \dot{\omega}_{LOSy} = -\frac{1}{r} a_{relz} - 2\frac{Vr}{r} \omega_{LOSy} + \omega_{LOSx} \omega_{LOSz} \quad (2-19)$$

$$P_{LOS} \dot{\omega}_{LOSz} = \frac{1}{r} a_{rely} - 2\frac{Vr}{r} \omega_{LOSz} + \omega_{LOSx} \omega_{LOSy} \quad (2-20)$$

Physical insight allows one to write a fourth scalar differential equation as,

$$P_{LOS} \dot{r} = Vr \quad (2-21)$$

where in eqns. (2-18) through (2-21):

r = range

Vr = range rate

a_{relx} = (acceleration of the target along the X_{LOS} axis minus acceleration of the tracker along the X_{LOS} axis); similarly for a_{rely} and a_{relz} .

As pointed out by Mitchell (Ref. 18:21), the angular velocities in the above state equations will be measured in the T-frame since there is no physical means of measuring in the LOS-frame. Additionally, the angular velocity about the line-of-sight, ω_{LOSx} , has no significance and must be eliminated from eqns. (2-19) and (2-20). It can be shown that ω_{LOSx} can be expressed as (Ref. 18:21),

$$\omega_{LOSx} = \omega_{Tx} + \delta\eta \omega_{Ty} - \delta\epsilon \omega_{Tz} \quad (2-22)$$

where, ω_{Tx} , ω_{Ty} , and ω_{Tz} are the inertial angular accelerations expressed in the T-frame. Substituting, eqn. (2-22) into eqns. (2-19) and (2-20) yields,

$$P_{LOS} \dot{\omega}_{LOSy} = -\frac{1}{r} a_{relz} - 2\frac{Vr}{r} \omega_{LOSy} + \omega_{LOSz} (\omega_{Tx} + \delta\eta \omega_{Ty} - \delta\epsilon \omega_{Tz})$$

and,

$$P_{LOS} \omega_{LOS_z} = \frac{1}{r} a_{rel_y} - 2 \frac{Y_r}{r} \omega_{LOS_z} - \omega_{LOS_y} (\omega_{Tx} + \delta \eta \omega_{Ty} - \delta \epsilon \omega_{Tz}) \quad (2-24)$$

The relative acceleration vector, \underline{a}_{rel} , is expressed in the LOS-frame; however, the accelerometer outputs for the tracker are available directly in T-frame coordinates while those of the target are expressed in b-frame coordinates. As a first step, the transformation from target accelerations to the LOS-frame can be accomplished by

$$\underline{a}_b^T = \underline{C}_b^T \underline{a}_b^b \quad (2-25)$$

where the transformation matrix \underline{C}_b^T is assumed known. Techniques for obtaining information about \underline{C}_b^T are discussed in the next section. Now the relative acceleration vector \underline{a}_r^T can be defined as

$$\underline{a}_r^T = \underline{a}_b^T - \underline{a}_T^T \quad (2-26)$$

Finally, using the transformation matrix \underline{C}_T^{LOS} defined in eqn. (2-11) yields the following expression for $\underline{a}_{rel}^{LOS}$

$$\underline{a}_{rel}^{LOS} = \underline{C}_T^{LOS} \underline{a}_r^T \quad (2-27)$$

Expanding eqn. (2-27), expressing it in component form, and substituting into eqns. (2-23), (2-24), and (2-18) gives

$$P_{LOS} Y_r = a_{rx} + r(\omega_{LOS_y}^2 + \omega_{LOS_z}^2) + \delta \eta a_{ry} - \delta \epsilon a_{rz} \quad (2-28)$$

$$P_{LOS} \omega_{LOS_y} = -\frac{1}{r} a_{rz} - 2 \frac{Y_r}{r} \omega_{LOS_y} + \omega_{LOS_z} \omega_{Tx} + \left[\frac{-\delta \epsilon}{r} a_{rx} + \omega_{LOS_z} (\delta \eta \omega_{Ty} - \delta \epsilon \omega_{Tz}) \right] \quad (2-29)$$

$$P_{LOS} \omega_{LOS_z} = \frac{1}{r} a_{ry} - 2 \frac{Y_r}{r} \omega_{LOS_z} - \omega_{LOS_y} \omega_{Tx} + \left[\frac{-\delta \eta}{r} a_{rx} - \omega_{LOS_y} (\delta \eta \omega_{Ty} - \delta \epsilon \omega_{Tz}) \right] \quad (2-30)$$

One additional modification to the above three state equations comes from substituting eqn. (2-9) into eqns. (2-28), (2-29), and (2-30). This gives,

$$P_{LOS} V_r = (f_{bx} - f_{Tx}) + (g_{bx} - g_{Tx})_{model} + \delta g_x + r(\omega_{LOS_y}^2 + \omega_{LOS_z}^2) + \delta \eta \delta g_y - \delta \epsilon \delta g_z + \epsilon_x \quad (2-31)$$

$$P_{LOS} \omega_{LOS_y} = -\frac{1}{r} [(f_{bz} - f_{Tz}) + (g_{bz} - g_{Tz})_{model} + \delta g_z] - \frac{2V_r}{r} \omega_{LOS_y} + \omega_{LOS_z} \omega_{Tx} + \epsilon_z + \left[-\frac{\delta \epsilon}{r} \delta g_x + \omega_{LOS_z} (\delta \eta \omega_{Ty} - \delta \epsilon \omega_{Tz}) \right] \quad (2-32)$$

$$P_{LOS} \omega_{LOS_z} = \frac{1}{r} [(f_{by} - f_{Ty}) + (g_{by} - g_{Ty})_{model} + \delta g_y] - \frac{2V_r}{r} \omega_{LOS_z} - \omega_{LOS_y} \omega_{Tx} + \epsilon_y + \left[-\frac{\delta \eta}{r} \delta g_x - \omega_{LOS_y} (\delta \eta \omega_{Ty} - \delta \epsilon \omega_{Tz}) \right] \quad (2-33)$$

It is assumed here that the tracker and target are both in the identical dynamic environment (i.e., vibration, bending, and other forces are the same on both bodies). Equations (2-31), (2-32), and (2-33) can then be rewritten as

$$P_{LOS} V_r = \delta g_x + r(\omega_{LOS_y}^2 + \omega_{LOS_z}^2) + \delta \eta \delta g_y - \delta \epsilon \delta g_z + \epsilon_x \quad (2-34)$$

$$P_{LOS} \omega_{LOS_y} = -\frac{\delta g_z}{r} - \frac{2V_r}{r} \omega_{LOS_y} + \omega_{LOS_z} \omega_{Tx} + \epsilon_z + \left[-\frac{\delta \epsilon}{r} \delta g_x + \omega_{LOS_z} (\delta \eta \omega_{Ty} - \delta \epsilon \omega_{Tz}) \right] \quad (2-35)$$

$$P_{LOS} \omega_{LOS_z} = \frac{\delta g_y}{r} - \frac{2V_r}{r} \omega_{LOS_z} - \omega_{LOS_y} \omega_{Tx} + \epsilon_y + \left[-\frac{\delta \eta}{r} \delta g_x - \omega_{LOS_y} (\delta \eta \omega_{Ty} - \delta \epsilon \omega_{Tz}) \right] \quad (2-36)$$

This assumption simplifies the dynamic simulation employed in the study, but it is not overly restrictive since non-field forces are sensed by the accelerometers and could thus be accounted for in actual practice.

The error angles, $\delta\eta$ and $\delta\epsilon$, appear in the above state equations and are a result of imperfect tracking. To estimate these two variables with the EKF it is necessary to develop state equations for them. In practice, the tracker will provide measurement information about $\delta\eta$ and $\delta\epsilon$, and the necessary state equations for these variables are given (with approximations) by Mitchell as (Ref. 18:19)

$$P_{LOS} \delta\eta = \omega_{LOSz} - \omega_{Tz} - \delta\epsilon \omega_{Tx} \quad (2-37)$$

$$P_{LOS} \delta\epsilon = \omega_{LOSy} - \omega_{Ty} + \delta\eta \omega_{Tx} \quad (2-38)$$

Six state equations have been developed in the preceding discussion, eqn. (2-21) and eqns. (2-34) through (2-38). However, in keeping with the objectives of this initial feasibility study, five of these six equations were simplified for application both in the truth model and in the filter.

In eqns. (2-34) through (2-38), the first simplification made was to neglect terms multiplied by $\delta\eta$ or $\delta\epsilon$. For the high accuracy tracking assumed here both $\delta\eta$ and $\delta\epsilon$ will have magnitudes on the order of 10^{-6} rad or smaller. For the profiles under test, the terms with brackets in eqns. (2-35) and (2-36) have magnitudes near 10^{-15} which are approximately 5 orders magnitude smaller than the magnitudes of $P_{LOS} \omega_{LOSy}$ and $P_{LOS} \omega_{LOSz}$. Also, in eqn. (2-34) the product terms

involving $\delta\eta$ and $\delta\epsilon$ have magnitudes near 10^{-13} while $P_{los} V_r$ has a magnitude near 10^{-8} . With these simplifications plus, the elimination of the ω_{Tx} terms (since torsional bending is negligible) yields the final six equations of the EKF.

$$P_{los} r = V_r \quad (2-39)$$

$$P_{los} V_r = \delta g_x + r(\omega_{losy}^2 + \omega_{losz}^2) + W_1 \quad (2-40)$$

$$P_{los} \omega_{losy} = \frac{-\delta g_x}{r} - 2\frac{V_r}{r} \omega_{losy} + W_2 \quad (2-41)$$

$$P_{los} \omega_{losz} = \frac{\delta g_y}{r} - 2\frac{V_r}{r} \omega_{losz} + W_3 \quad (2-42)$$

$$P_{los} \delta\eta = \omega_{losz} - \omega_{Tz} + W_4 \quad (2-43)$$

$$P_{los} \delta\epsilon = \omega_{losy} - \omega_{Ty} + W_5 \quad (2-44)$$

where W_1 through W_5 are zero-mean white Gaussian noises added to account for the neglected terms. All that remains is to develop the stochastic process models for the δg components.

In this study, the estimation problem is formulated in state-space with a dynamics model satisfying a stochastic differential equation. It is appropriate, therefore, to seek a stochastic model for the δg components. Typically the anomalous gravity field or "disturbance" model is separated into north and east deflections of the vertical and a gravity anomaly component (see, for example, Ref. 26:135-142). As shown in Fig. 6, the vertical deflections are defined as the angular deviations between the true gravity vector \underline{g}_{True} , which is normal to the geoid, and the reference gravity

vector, g_{Ref} , which is normal to the reference ellipsoid. The geoid represents a surface of constant gravitational potential, and the difference in height between the geoid and the reference ellipsoid surface is called the geoid height or undulation, N .

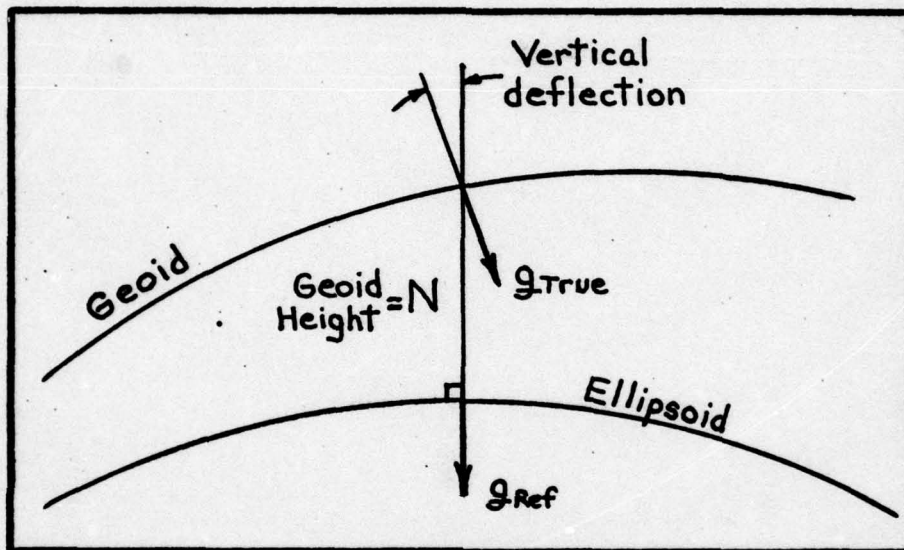


Fig. 6 Gravity Disturbance Quantities
(Ref. 4:111)

Several stochastic models for the disturbance components can be found in the literature. Musick in Reference 19 presents synopses of seven papers describing different statistical models. The most basic disturbance model assumes that a first-order Markov process adequately characterizes the disturbance components. This model has some physical appeal as it does account for the spatial correlation of gravity disturbances that is observed in nature (e.g., see Ref. 26: 135-138). Carlson, as reported in Reference 26:136, has

suggested that an appropriate model is the sum of a first-order Markov process plus a random bias. Other models, such as the second-order Markov model proposed by Kasper (Ref. 13), are higher-order models which attempt to model more closely the empirical disturbance data. The disadvantage, of course, in using the higher-order models in an on-line estimator is the increase in state vector dimension as the order of the disturbance model increases. For this reason, a first-order Markov process model was chosen for use in this study, although any subsequent work to this study should investigate the benefits to be derived from the higher-order models. It may also be quite appropriate to use different statistical models for the downrange, crossrange, and vertical directions.

The first-order Markov process can be generated by passing white noise through a first-order lag as shown in Fig. 7. The autocorrelation, Ψ_{xx} , and power spectral density, $\bar{\Psi}_{xx}$, functions for this exponentially time correlated process are shown in Fig. 8.

In reality gravity disturbances are spatially correlated and not intrinsically time correlated. Nevertheless, one can transform a spatially correlated process into a time correlated process and vice versa by relating time and distance through the vehicle's velocity variable (assuming constant velocity) (i.e., $d = vT$, where d is distance, v is velocity, and T is time). If this is done, then the expression for the autocorrelation function shown in Fig. 8 becomes,

$$\Psi_{xx}(d) = \sigma_x^2 e^{-|d|/D}$$

(2-45)

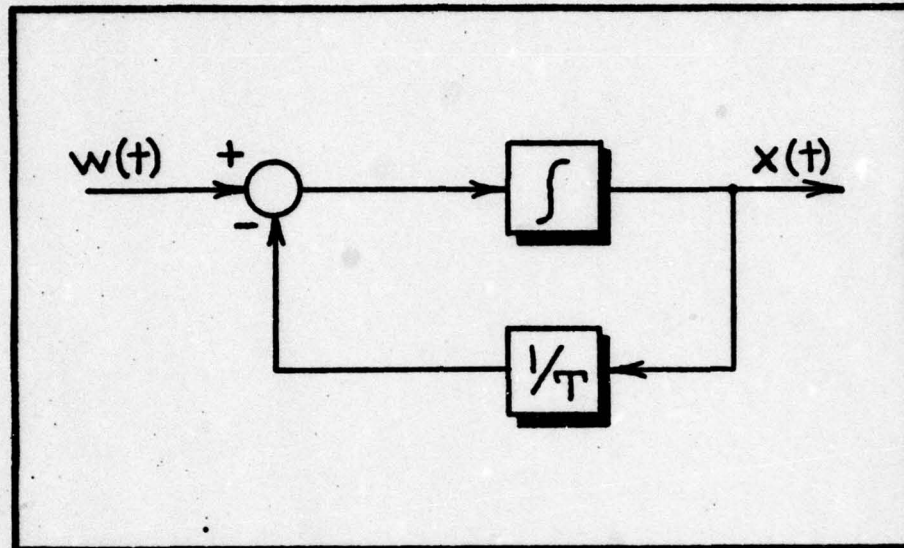


Fig. 7 First-Order Markov Shaping Filter
(shaded box convention is used in Ref. 6)

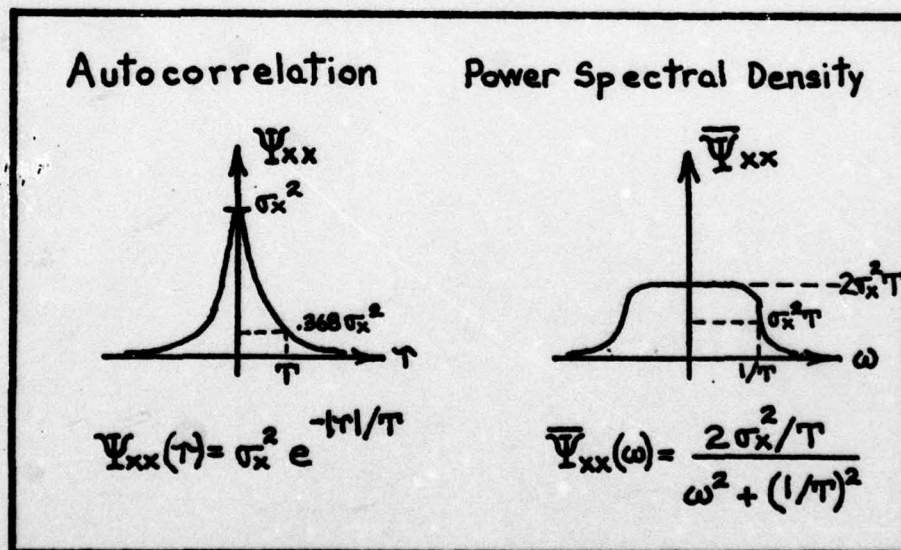


Fig. 8 Autocorrelation and Power Spectral Density
Functions for First-Order Markov Process
(Ref. 13:Chap 4, p. 85)

where D is the correlation distance and σ_x is the standard deviation. Widnall and Grundy (Ref. 26:137) give the following values for the standard deviation and correlation distance for each of the three disturbance components for the western U.S. assuming zero correlation between components.

Table II. Gravity Variations for Western U.S.

Component	σ (μg)	D (nmi.)
east-west deflection	26	10
north-south deflection	17	10
anomaly (magnitude)	35	60

Up until this point, all of the gravity disturbance models discussed are meant to model the disturbance along one particular trajectory. The situation in this problem, however, is to model the difference in disturbance between two trajectories only 10 meters apart. Since differential disturbance models are not available in the literature, it was decided to do a spectral analysis of the empirical gravity data and to propose an appropriate shaping filter to generate a process with the same statistics.

The power spectral density (PSD) plots generated from the limited data samples available can be found in Appendix C along with a discussion of how they were generated. As a result of this analysis, a first-order Markov process model was chosen for the 10,000 foot altitude case.

The state variable equations for the three disturbance components based on a first-order Markov model can now be

written as,

$$\dot{\delta g}_x = -\frac{1}{T_x} \delta g_x(t) + w_1(t) \quad (2-46a)$$

$$\dot{\delta g}_y = -\frac{1}{T_y} \delta g_y(t) + w_2(t) \quad (2-46b)$$

$$\dot{\delta g}_z = -\frac{1}{T_z} \delta g_z(t) + w_3(t) \quad (2-46c)$$

where: T_x , T_y , and T_z = correlation times for the δg_x , δg_y , and δg_z processes respectively, and

$w_1(t), w_2(t), w_3(t)$ = zero-mean mutually independent white Gaussian noises with statistics

$$E\{w_1(t)w_1^T(t+\tau)\} = q_1(t)\delta(\tau)$$

$$E\{w_2(t)w_2^T(t+\tau)\} = q_2(t)\delta(\tau)$$

$$E\{w_3(t)w_3^T(t+\tau)\} = q_3(t)\delta(\tau)$$

Figure 9 is a plot of the true δg components for the 10,000 foot altitude simulation. The curve was plotted from data obtained from GTGRV. It represents the gravitational accelerations due only to point masses in the GTGRV model for a vehicle at 10,000 feet flying at a speed of 100 mi/hr. The data was obtained at 10 sec intervals. The sawtooth effect in the curves is a result of the sampling scheme employed. Note that the magnitudes of the δg components for the time period of interest are $< 2 \times 10^{-2}$ mgal, considerably smaller than the disturbance values given in Table II. The reason for this is that the data in Fig. 9 represents the

differential disturbances for two objects only 10 meters apart, whereas, Table II values are for one object. These small disturbance magnitudes contributed to the problems which attended this study.

As plotted, the $\delta \underline{g}$ components are expressed in LOS-frame coordinates although they were initially output by GTGRV in e-frame coordinates. The coordinate transformation matrix used in this case is

$$\underline{C}_e^{LOS} = \begin{bmatrix} -1 & 0 & 0 \\ 0 & 1 & 0 \\ 0 & 0 & -1 \end{bmatrix} \quad (2-47)$$

Although in reality \underline{C}_e^{LOS} is not time-variant, for the short duration of this simulation (745 sec for the 10,000 foot altitude case) compared to the dynamics of the system, eqn. (2-47) remains valid. It is hoped that a first-order Markov model is an adequate model for the $\delta \underline{g}$ components in Fig. 9.

In contrast to the obvious periodicity of the $\delta \underline{g}$ components in the high altitude, high speed (relative to 6 knots) case of Fig. 9, the $\delta \underline{g}$ components for the 0 ft. altitude, 6 knot case are plotted in Fig. 10. Note that, although one knows in reality that $\delta \underline{g}$ in this case is also time-correlated, the duration of the simulation is much less than the correlation time. In view of this, it was decided to change the model for the $\delta \underline{g}$ components in the 0 ft. altitude case from a first-order Markov model to a random bias model, although

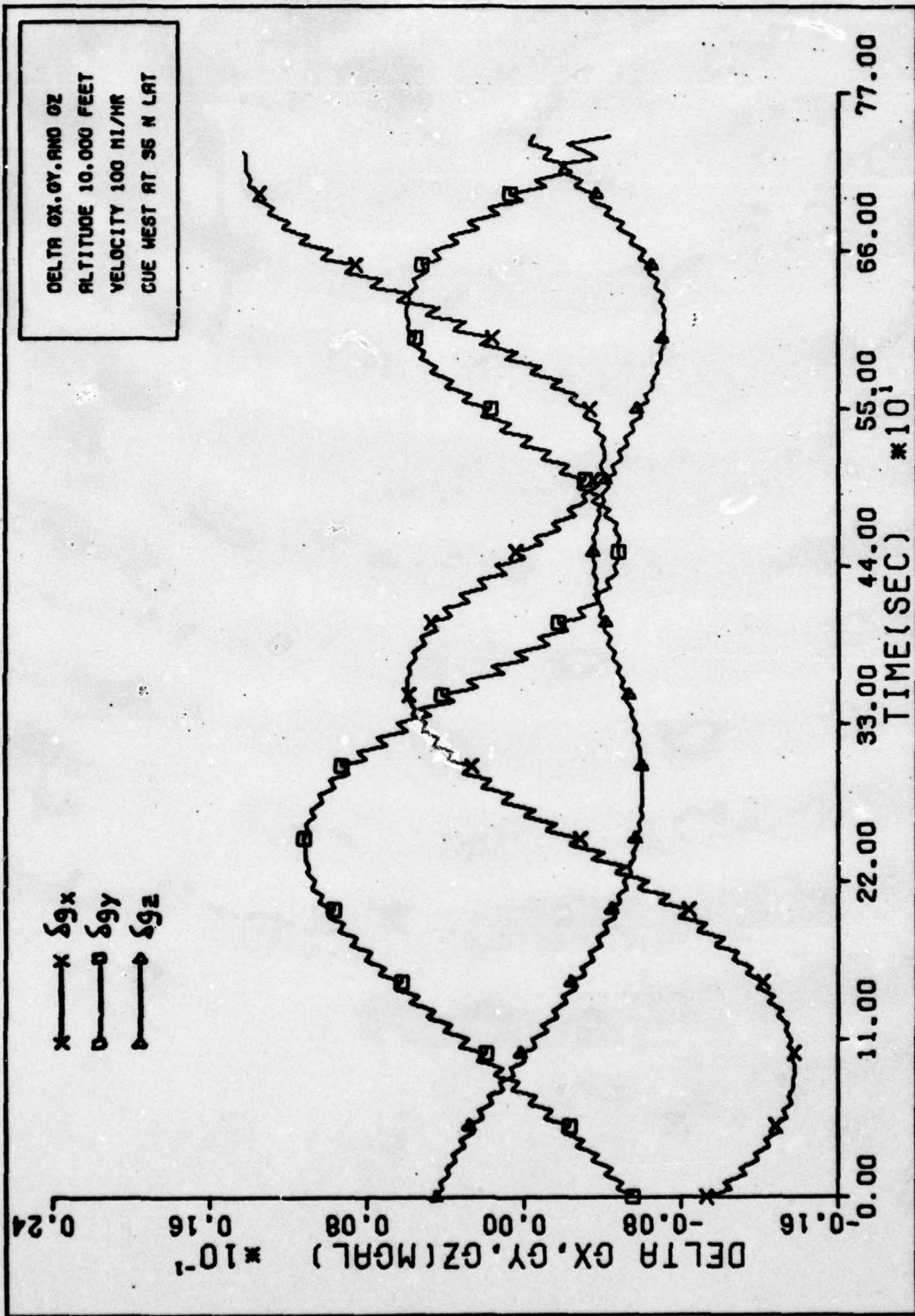


FIG. 9 TRUE DELTA GX, GY, AND GZ (10,000 feet)

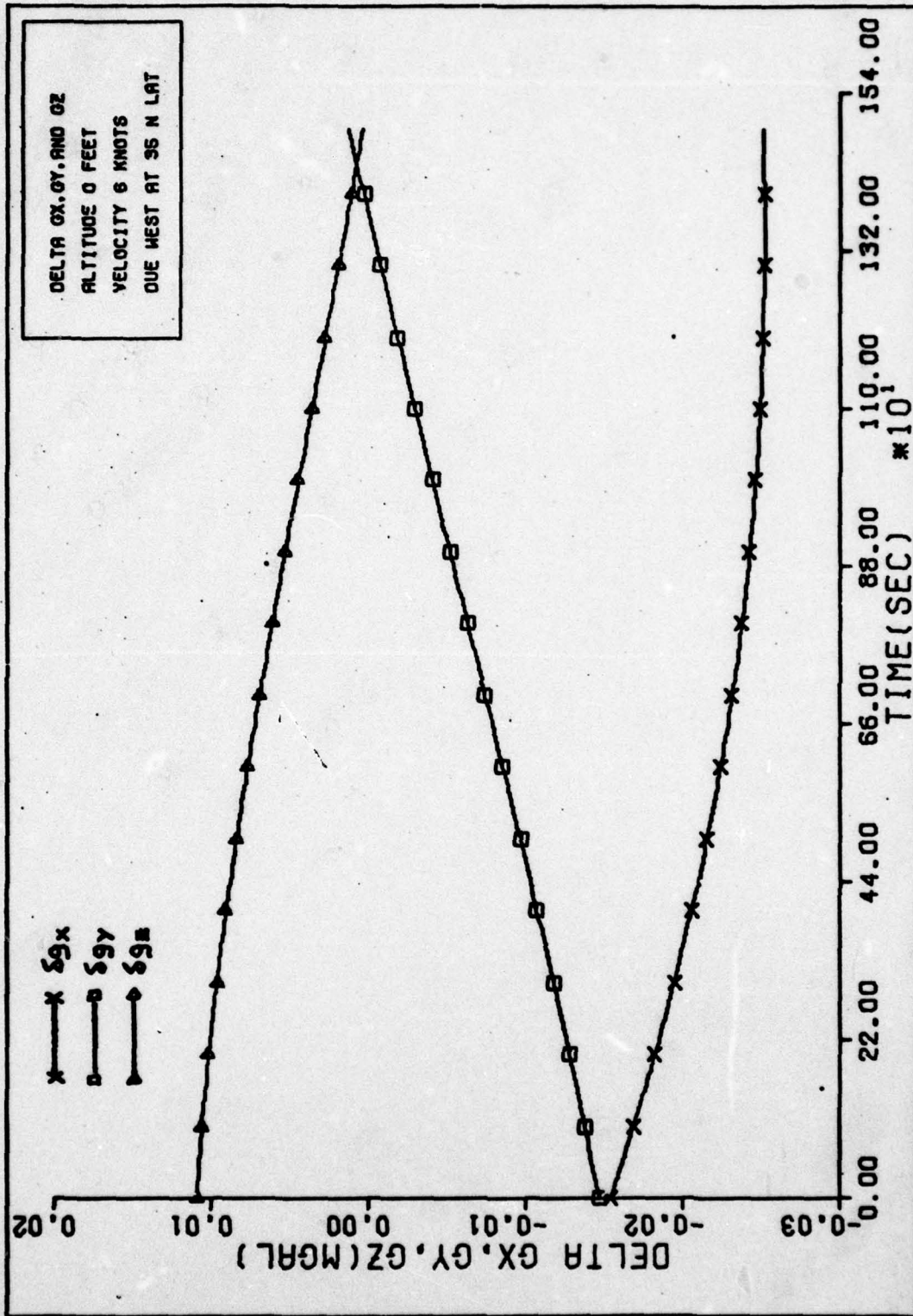


FIG. 10 TRUE DELTA GX, GY, AND GZ (0 feet)

the original model is still valid. A random bias process can be generated as the output of an integrator with no input other than an initial condition. The describing differential equation is given by

$$\dot{x}(t) = 0 \quad (2-48)$$

In the actual simulation, a pseudonoise, a low strength white Gaussian noise, was added to this model to insure that the EKF would track the slowly changing bias.

The shaping filter for this process is shown in Fig. 11 and the autocorrelation and power spectral density functions for this process are shown in Fig. 12.

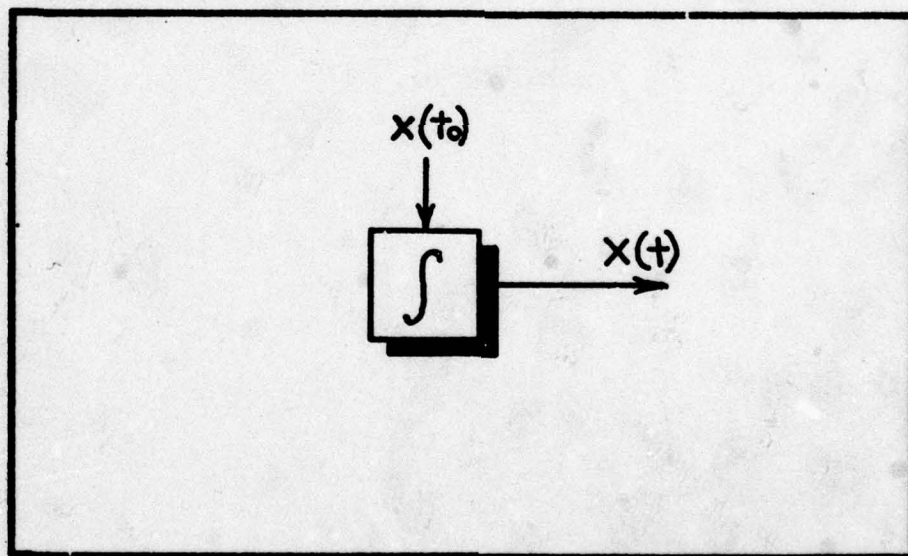


Fig. 11 Shaping Filter for Random Bias

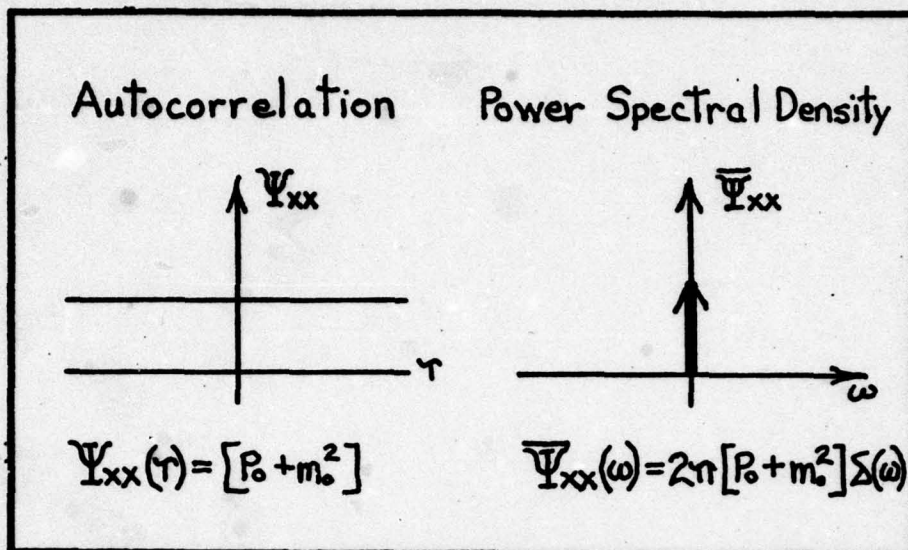


Fig. 12 Autocorrelation and Power Spectral Density Functions for Random Bias
(Ref. 15: Chap 4, p. 85)

Measurement Equations

Only three measurements are assumed in this study - measurements of range and the tracking angular deviations, $\delta\eta$ and $\delta\epsilon$. In keeping with the simplifying assumptions made throughout this study, the range measurement is assumed to be the true range value corrupted by a white Gaussian noise. Thus,

$$r_m = r_{\text{True}} + v_1 \quad (2-49)$$

where, v_1 is a zero-mean white Gaussian noise with standard deviation of $1 \times 10^{-5} \text{m}$. A more realistic measurement model would depend upon the type of instrument used, but for the purpose of this generic study eqn. (2-49) suffices.

The measurements of $\delta\eta$ and $\delta\epsilon$ will not truly be measurements at all in the sense that they represent a true value

plus some corruption. It will be remembered that $\delta\eta$ and $\delta\epsilon$ were equal to zero for all time in the truth model. Instead, $\delta\eta$ and $\delta\epsilon$ "measurements" are generated as samples from white Gaussian noise processes, each with a standard deviation (1σ) of $1\mu\text{rad}$. Thus,

$$\delta\eta = v_2 \quad (2-50a)$$

$$\delta\epsilon = v_3 \quad (2-50b)$$

The values for system parameters, ω_{Ty} and ω_{Tz} , were generated by adding white Gaussian noise with $\sigma = 10^{-7}$ to the true values of ω_{Losy} and ω_{Losz} .

The assumption here, of course, is that the angular rate sensors on the tracker produce measurements that can be expressed as,

$$\omega_{Ty} = \omega_{Losy} + v_4 \quad (2-51a)$$

$$\omega_{Tz} = \omega_{Losz} + v_5 \quad (2-51b)$$

Once again, a very simplistic model for angular rate errors is assumed. It should be recognized that more detailed modelling would be necessary in an evaluation of a particular hardware configuration.

Hardware Configurations

This discussion will include a general description of some of the system components and will illustrate some potential measurement techniques. No attempt is made to present a detailed hardware design, however, as that is beyond the scope of this study.

To begin with, the range measurement is important to the overall accuracy of the gradient estimation process because

of its appearance in eqn. (2-10). One possible source of relative range measurements is an interferometer shown in Fig. 13.

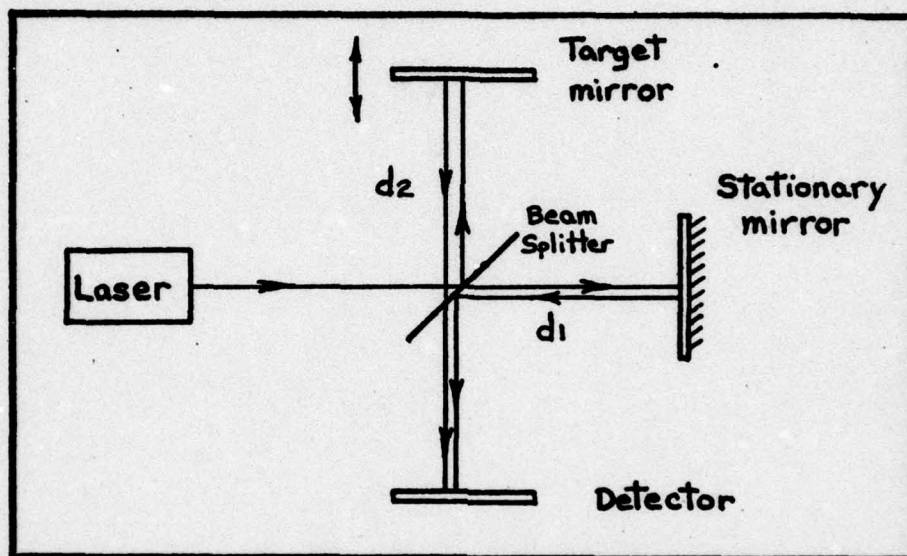


Fig. 13 Interferometer (Ref. 7:1091)

In Fig. 13, a laser produces a narrow beam of monochromatic light. At the beam-splitter, one-half of the incident light is reflected toward the target mirror and one-half toward the stationary mirror. If the two mirrors are each an integral number of wavelengths from the beam-splitter, the reflected light arrives at the detector in phase and a bright spot is detected. If on the other hand, the target mirror moves one-half of a wavelength, then destructive interference occurs and no light, or very little light, reaches the detector. Thus, the intensity variations of light at the detector can be used to infer relative movement between the target and

the beam-splitter. The device as just described would be very sensitive to changes in the characteristics of the optical path medium (e.g., changes in the index of refraction), thermal or other distortions in the mirrors and beam-splitter, and vibration. Evacuating the light pathways would alleviate problems of the first kind. Proper environmental controls and manufacturing processes could minimize problems of the second kind. However, isolating the device from vibration, especially in a moving vehicle such as an aircraft or submarine, represents a formidable challenge and may be the limiting factor in an operational system.

It remains for the tracker to measure the misalignment angles between the LOS and T-coordinate frames. This could, perhaps, be performed by the same instrument designed to obtain the relative range measurements discussed above. One interesting technique for accomplishing this is described in Reference 8. The instrument, called STARTRAC, provides angular deviation measurements between star LOS and stable member mirror normal in two degrees of rotational freedom (Ref. 8:Section 1, p.4). A simplified diagram of STARTRAC is shown in Fig. 14.

In Fig. 14, the stable member mirror could be mounted on the tracker with the normal to its surface being colinear with the x_T -axis. A light source on the target, or a reflector mounted on the target to return light generated by the tracker, would provide a signal to the star tracker whose outputs would indicate the angular deviations of the x_T -axis

from the x_{LOS} -axis.

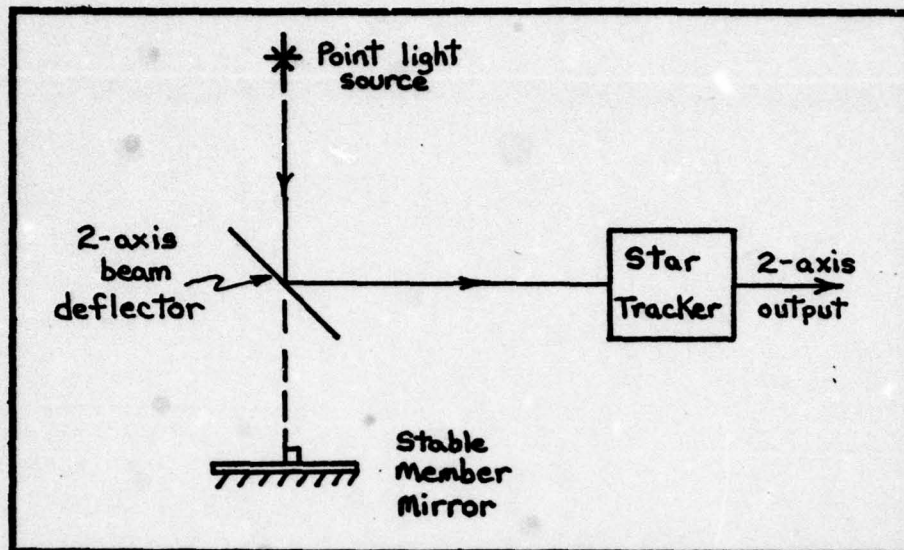


Fig. 14 Basic STARTRAC Concept (Ref. 7:1-4)

An associated problem is that of determining the attitude of the target platform relative to the tracker's coordinate frame. A device to sense the angular orientation of the platform frame with respect to the tracker could be an autocollimator. Such a device is depicted in Fig. 15.

In an autocollimator a collimated beam of light is reflected off a mirror on the target and the return beam is passed through the same optics and focused on a photodetector. The displacement at the detector between the reflected image and the effective location of the light source is a measure of the misalignment between the units (Ref. 9:17). Harris, et al, (Ref. 9:36-42) discuss two systems under development to accomplish 3-axis optical angular measurements—the Chrysler-Optical Angular Motion Sensor and the Barnes

Flexure Monitor System. Of the two systems, the Chrysler system is reported to have the potential of $< 5 \text{ } \overline{\text{sec}}$ accuracy over distances greater than 50 feet and the Barnes system is said to have accuracy of $0.28 \text{ } \overline{\text{sec}}$ over a distance of 5 feet (Ref. 9:37). A third system mentioned briefly in Reference 9 is the Martin Universal Star Tracker which employs a correlation tracker using stored maps of the light sources being tracked (Ref. 9:40). At this point, the tracker hardware to accomplish range, angle, and coordinate frame misalignment measurements has been briefly discussed. A discussion of the accelerometers in the system follows.

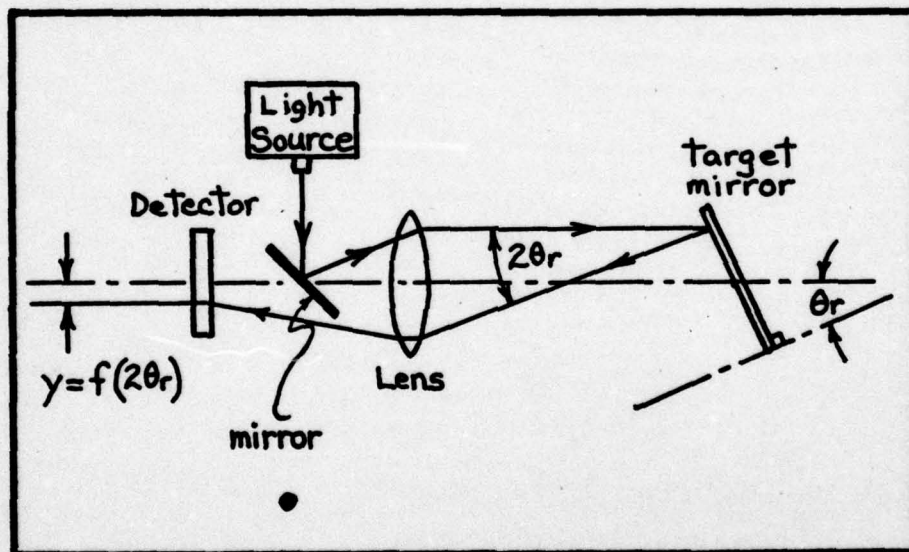


Fig. 15 Autocollimator (Ref. 9:17)

As stated by Slater, "The integrating type of accelerometer is particularly attractive for gravity measurements on an unstable base such as a ship because accelerations associated with rolling and pitching are effectively averaged out."

(Ref. 24:196). Slater goes on to point out that bias stability is the most important consideration in gravimetry. A substantial bias component in accelerometer output would effectively mask out any gravitational disturbance variations unless the bias could be compensated for. Although in this study, accelerometer errors are modelled as white Gaussian noise, it is recognized that any operational system based on this proposal would probably augment the state vector to include estimating the bias, scale factor errors, and other non-linearities in the accelerometers.

In addition to the above considerations, it should be recognized that acceleration components associated with the vehicle's movement through the air or water must be known to the same degree of accuracy as desired for the gravity disturbances. Slater in Reference 24 published in 1964, states that accelerometer sensitivities of 10^{-8} m/sec² had been demonstrated for earth-based gravimeters. This is on the order of the anomalous relative gravitational accelerations encountered in this study, and offers encouragement for the practical application of the gradient mapping system proposed here.

This concludes the brief discussion of the hardware which might be used in a practical system as envisioned here. The EKF formulation is discussed next.

III. Extended Kalman Filter

Formulation (Ref. 15)

It is assumed that the reader has an understanding of linear Kalman filters and is familiar with the filter equations. Consequently, the discussion which follows will begin with a statement of the state dynamics model for the EKF and will conclude with a description of the EKF equations. No attempt is made to derive the EKF formulation, but the interested reader is referred to Ref. 6 or Ref. 15 for such details.

The EKF is one method used in estimation problems where nonlinearities in the deterministic portion of the state dynamics and measurement models cannot be neglected. In this study, the state equations are continuous in time, but measurements will be incorporated at discrete intervals. For this reason, the continuous form of the EKF with discrete measurement updates is appropriate.

Let the system state equations satisfy the following nonlinear vector stochastic differential equation written in the familiar white noise notation as

$$\dot{\underline{x}}(t) = \underline{f}[\underline{x}(t), t] + \underline{G}(t)\underline{w}(t) \quad (3-1)$$

where:

$\dot{\underline{x}}(t)$ = time derivative of the system state
n-vector at time t,

$\underline{f}[\underline{x}(t), t]$ = n-vector of nonlinear system dynamics,

$\underline{G}(t)$ = system noise input matrix, and
 $\underline{w}(t)$ = Gaussian white noise vector with statistics

$$E\{\underline{w}(t)\} = \underline{0}$$

$$E\{\underline{w}(t)\underline{w}^T(t+\tau)\} = \underline{Q}(t)\delta(\tau)$$

The initial conditions for the state vector $\underline{x}(t_0)$ is assumed to be a Gaussian random vector with mean $\hat{\underline{x}}_0$ and covariance matrix \underline{P}_0 . The carat symbol, or "hat," over a quantity represents an estimate of that quantity, not, in general, its true value.

Let the discrete-time measurement equations satisfy the following nonlinear vector equation

$$\underline{z}(t_i) = \underline{h}[\underline{x}(t_i), t_i] + \underline{v}(t_i) \quad (3-2)$$

where:

$\underline{z}(t_i)$ = m-vector of measurements at time t_i ,
 $\underline{h}[\underline{x}(t_i), t_i]$ = vector of nonlinear functions of states and current time t_i , and
 $\underline{v}(t_i)$ = Gaussian white noise vector with statistics

$$E\{\underline{v}(t_i)\} = \underline{0}$$

$$E\{\underline{v}(t_i)\underline{v}^T(t_j)\} = \begin{cases} \underline{R}(t_i) & , t_i = t_j \\ \underline{0} & , t_i \neq t_j \end{cases}$$

With the system dynamics and measurement models given in eqns. (3-1) and (3-2), one desires an optimal state estimate. In the case of linear systems this optimal estimate can be shown to be that of the Kalman filter. To extend the Kalman filter

formulation to the nonlinear case, as is done here, one seeks to linearize about some reference trajectory. One can then employ linear perturbation techniques which, although they will not result in an "optimal" estimate, will produce sufficiently accurate results. Of course, the accuracy of the resulting estimate depends directly on how small are the deviations from the reference (nominal) trajectory. To enhance the validity of the assumption that linear perturbation techniques can provide adequate results, the EKF relinearizes about each new estimate $\hat{\underline{x}}(t_i^+)$ as it is computed. The plus (+) sign superscript indicates a quantity computed after the measurements just made are incorporated. A minus sign (-) superscript refers to quantities computed just prior to measurement updating.

The EKF equations will now be given. The state estimate is propagated forward from time t_i to the next sample time t_{i+1} by integrating

$$\dot{\hat{\underline{x}}}(t/t_i) = \underline{f}[\hat{\underline{x}}(t/t_i), t] \quad (3-3)$$

$$\begin{aligned} \dot{\underline{P}}(t/t_i) = & \underline{F}[\hat{\underline{x}}(t/t_i), t] \underline{P}(t/t_i) + \underline{P}(t/t_i) \underline{F}^T[\hat{\underline{x}}(t/t_i), t] \\ & + \underline{G}(t) \underline{Q}(t) \underline{G}^T(t) \end{aligned} \quad (3-4)$$

from initial conditions given by

$$\hat{\underline{x}}(t_i/t_i) = \hat{\underline{x}}(t_i^+) \quad (3-5)$$

$$\underline{P}(t_i/t_i) = \underline{P}(t_i^+) \quad (3-6)$$

(From t_0 to t_1 , the first time interval, the initial conditions

are $\hat{\underline{x}}_0$ and \underline{P}_0). In eqn. (3-4) above, $\underline{F}[\hat{\underline{x}}(t/t_i), t]$ is defined as the n-by-n partial derivative matrix:

$$\underline{F}[\hat{\underline{x}}(t/t_i), t] \triangleq \left. \frac{\partial f[\underline{x}, t]}{\partial \underline{x}} \right|_{\underline{x} = \hat{\underline{x}}(t/t_i)} \quad (3-7)$$

After integrating eqns. (3-3) and (3-4) to time t_{i+1} , $\hat{\underline{x}}(t_{i+1}^-)$ and $\underline{P}(t_{i+1}^-)$ are defined as:

$$\hat{\underline{x}}(t_{i+1}^-) = \hat{\underline{x}}(t_{i+1}/t_i) \quad (3-8)$$

$$\underline{P}(t_{i+1}^-) = \underline{P}(t_{i+1}/t_i) \quad (3-9)$$

and used in the next measurement update.

The system measurements, \underline{z}_i , are incorporated in the EKF by

$$\underline{K}(t_i) = \underline{P}(t_i^-) \underline{H}^T[\hat{\underline{x}}(t_i^-); t_i] \{ \underline{H}[\hat{\underline{x}}(t_i^-); t_i] \underline{P}(t_i^-) \underline{H}^T[\hat{\underline{x}}(t_i^-); t_i] + \underline{R}(t_i) \}^{-1} \quad (3-8)$$

$$\hat{\underline{x}}(t_i^+) = \hat{\underline{x}}(t_i^-) + \underline{K}(t_i) \{ \underline{z}_i - \underline{h}[\hat{\underline{x}}(t_i^-); t_i] \} \quad (3-9)$$

$$\underline{P}(t_i^+) = \underline{P}(t_i^-) - \underline{K}(t_i) \underline{H}[\hat{\underline{x}}(t_i^-); t_i] \underline{P}(t_i^-) \quad (3-10)$$

where $\underline{H}[\hat{\underline{x}}(t_i^-); t_i]$ is defined as the m-by-n partial derivative matrix:

$$\underline{H}[\hat{\underline{x}}(t_i^-); t_i] \triangleq \left. \frac{\partial h[\underline{x}, t_i]}{\partial \underline{x}} \right|_{\underline{x} = \hat{\underline{x}}(t_i^-)} \quad (3-11)$$

and $\underline{K}(t_i)$ is the n-by-m Kalman gain matrix. With the basic EKF formulation completed, one can turn his attention to applying this non-linear estimator to the problem under study.

Application to this Problem

The state equations upon which the estimator is based are restated here using slightly different notation from

that used in Chapter II. The 9-state vector, $\underline{x}(t)$, is given by (dropping the time argument for convenience)

$$\underline{x} = \begin{bmatrix} X_1 \\ X_2 \\ X_3 \\ X_4 \\ X_5 \\ X_6 \\ X_7 \\ X_8 \\ X_9 \end{bmatrix} = \begin{bmatrix} r \\ V_r \\ \omega_{LOS_y} \\ \omega_{LOS_z} \\ \delta\pi \\ \delta e \\ \delta g_x \\ \delta g_y \\ \delta g_z \end{bmatrix} \quad (3-12)$$

where \underline{x} is modelled as a Gaussian random vector with initial conditions \underline{x}_0 and \underline{P}_0 . The non-linear state dynamics can be written as

$$\underline{f}[\underline{x}(t_i), t_i] = \begin{bmatrix} X_2 \\ X_1(X_3^2 + X_4^2) + X_7 \\ \frac{-2X_2X_3 - X_9}{X_1} \\ \frac{-2X_2X_4 + X_8}{X_1} \\ X_4 - \omega_{T_z} \\ X_3 - \omega_{T_y} \\ -\frac{1}{T_x} X_7 \\ -\frac{1}{T_y} X_8 \\ -\frac{1}{T_z} X_9 \end{bmatrix} \quad (3-13)$$

while the additive state dynamics driving noise term,

$\underline{G}(t)\underline{w}(t)$, is given by

$$\underline{G}(t)\underline{w}(t) = \begin{bmatrix} 0 \\ w_1 \\ w_2 \\ w_3 \\ w_4 \\ w_5 \\ w_6 \\ w_7 \\ w_8 \end{bmatrix} \quad (3-14)$$

where $\underline{G}(t)$ is a 9x9 identity matrix and $\underline{w}(t)$ is a 9-vector with a zero as the first element. The $\underline{w}(t)$ vector has statistics

$$E\{\underline{w}(t)\} = \underline{0} \quad (3-15)$$

$$E\{\underline{w}(t)\underline{w}^T(t+\tau)\} = \underline{Q}(t)\delta(\tau)$$

where $\underline{Q}(t)$ is

$$\underline{Q}(t) = \begin{bmatrix} 0 & & & & & & & & \\ & q_{22} & & & & & & & \\ & & q_{33} & & & & & & \\ & & & q_{44} & & & & & \\ & & & & q_{55} & & & & \\ & & & & & q_{66} & & & \\ & & & & & & q_{77} & & \\ & & & & & & & q_{88} & \\ & & & & & & & & q_{99} \end{bmatrix} \quad (3-16)$$

and $\delta(\tau)$ is the Dirac delta function. Numerical values used

in the filter for \underline{x}_0 , \underline{P}_0 , and $\underline{Q}(t)$ can be found in Appendix B.

The measurements, as discussed in Chapter II, are linear measurements of states x_1 , x_5 , and x_6 and satisfy the equation

$$\underline{z}(t_i) = \underline{H} \underline{x}(t_i) + \underline{v}(t_i) \quad (3-17)$$

For this problem, $\underline{H} \underline{x}(t_i)$ is expressed as

$$\underline{H} \underline{x}(t_i) = \begin{bmatrix} x_1(t_i) \\ x_5(t_i) \\ x_6(t_i) \end{bmatrix} \quad (3-18)$$

and the measurement corruption noise vector $\underline{v}(t_i)$ has statistics

$$\begin{aligned} E\{\underline{v}(t_i)\} &= \underline{0} \\ E\{\underline{v}(t_i) \underline{v}^T(t_j)\} &= \begin{cases} \underline{R}(t_i), & t_i = t_j \\ \underline{0}, & t_i \neq t_j \end{cases} \end{aligned} \quad (3-19)$$

where $\underline{R}(t_i)$ is given by

$$\underline{R}(t_i) = \begin{bmatrix} r_{11} & 0 & 0 \\ 0 & r_{22} & 0 \\ 0 & 0 & r_{33} \end{bmatrix} \quad (3-20)$$

Numerical values for $\underline{R}(t_i)$ are also given in Appendix B.

Finally, two additional matrices must be defined before the EKF can be used in a simulation. These matrices are

$\underline{H}[\underline{\hat{x}}(t_i^-); t_i]$ defined in eqn. (3-11) and $\underline{F}[\underline{\hat{x}}(t/t_i), t]$ defined in eqn. (3-7). For this problem $\underline{F}[\underline{\hat{x}}(t/t_i), t]$ can be expressed as that shown in Figure 16, and $\underline{H}[\underline{\hat{x}}(t_i^-); t_i]$ is

$$\underline{H} = \begin{bmatrix} 1 & 0 & 0 & 0 & 0 & 0 & 0 & 0 & 0 \\ 0 & 0 & 0 & 0 & 1 & 0 & 0 & 0 & 0 \\ 0 & 0 & 0 & 0 & 0 & 1 & 0 & 0 & 0 \end{bmatrix} \quad (3-22)$$

With all of the pieces developed that are needed to operate the EKF, the simulation begins by propagating eqns. (3-3) and (3-4) forward one time interval (10 sec was used here). The 10 sec interval was chosen because the δg data was available at 10 sec intervals. The propagation of the state estimate, $\underline{\hat{x}}(t)$, and covariance matrix, $\underline{P}(t)$, was accomplished by direct numerical integration of eqns. (3-3) and (3-4). The integration package used was ODE, an ordinary differential equation solver which is part of the CDC 6600 library of subroutines at the Aeronautical Systems Division Computer Center. ODE utilizes a modified divided difference form of the Adams Pece formulas and local extrapolation. It adjusts the order and step size to control the local error per unit step. The interested reader is referred to Reference 20 for more details on this computer program.

At the end of the first time interval, ODE returns the state vector and covariance matrix, $\underline{\hat{x}}(t_i^-)$ and $\underline{P}(t_i^-)$ respectively. At this point system measurements are taken. These measurements are incorporated into the EKF and used to improve the state and covariance estimates. Equations (3-8), (3-9),

$$F_1 = \begin{bmatrix} 0 & 0 & -\frac{1}{\hat{x}_1} & 0 & 0 & 0 & 0 & 0 & 0 & -1/\sqrt{\pi_z} \\ 0 & 0 & 0 & \frac{1}{\hat{x}_1} & 0 & 0 & 0 & 0 & -1/\sqrt{\pi_y} & 0 \\ 0 & 1 & 0 & 0 & 0 & 0 & 0 & -1/\sqrt{\pi_x} & 0 & 0 \\ 0 & 0 & 0 & 0 & 0 & 0 & 0 & 0 & 0 & 0 \\ 0 & 0 & 0 & 0 & 0 & 0 & 0 & 0 & 0 & 0 \\ 0 & 2\hat{x}_1\hat{x}_4 & 0 & -\frac{2\hat{x}_2}{\hat{x}_1} & 1 & 0 & 0 & 0 & 0 & 0 \\ 0 & 2\hat{x}_1\hat{x}_3 & -\frac{2\hat{x}_2}{\hat{x}_1} & 0 & 0 & 1 & 0 & 0 & 0 & 0 \\ 1 & 0 & -\frac{2\hat{x}_3}{\hat{x}_1} & -\frac{2\hat{x}_4}{\hat{x}_1} & 0 & 0 & 0 & 0 & 0 & 0 \\ 0 & \frac{\hat{x}_3^2 + \hat{x}_4^2}{\hat{x}_1^2} & \frac{2\hat{x}_2\hat{x}_3 + \hat{x}_3}{\hat{x}_1^2} & \frac{2\hat{x}_2\hat{x}_4 - \hat{x}_3}{\hat{x}_1^2} & 0 & 0 & 0 & 0 & 0 & 0 \end{bmatrix}$$

Fig. 16 F Matrix for EKF

and (3-10) are typically used in measurement updating, however, for this problem an alternate form of eqn. (3-10) was selected initially. This alternate form of the covariance matrix update equation is sometimes called the "Joseph form" and is given by (Ref. 6:305)

$$\underline{P}^+ = (\underline{I} - \underline{K}\underline{H})\underline{P}^-(\underline{I} - \underline{K}\underline{H})^T + \underline{K}\underline{R}\underline{K}^T \quad (3-23)$$

where the time argument is again dropped for convenience. Although eqn. (3-23) involves more computation time than eqn. (3-10), it is inherently more accurate and it was on this basis that the Joseph form was selected initially for this filter. Unfortunately, despite its accuracy, covariance measurement updating by eqn. (3-23) does not insure retaining positive semidefiniteness of the error covariance. This loss of positive semidefiniteness was observed during the first few simulation runs. As stated by Maybeck (Ref. 16:12), it can be shown that the Kalman filter algorithm is numerically unstable. Truncation errors due to finite wordlength are thus propagated once they occur and do not die out. In this case, a CDC 6600 computer with a 60-bit wordlength was used; however, even with this large a wordlength numerical instability in the algorithm was observed. Such problems often occur when, as Maybeck puts it:

"... (1) the measurements are very accurate (eigenvalues of $\underline{R}(t_i)$ are small relative to those of $\underline{P}(t_i^-)$, this being accentuated by large eigenvalues in \underline{P}^0) or (2) a linear combination of state vector components is known with great precision while other combinations are nearly unobservable (i.e., there is a large range of magnitudes of state covariance eigenvalues." (Ref. 16:12,13)

Certainly in this application condition (1) above applies. What, then are the possible solutions to this problem ?

Traditional solutions to the inherent numeric problems of the Kalman filter include performing measurement updating in double precision, scaling variables to reduce dynamic range, or employing ad hoc modifications (e.g., placing lower limits on covariance diagonal terms or upper limits on off-diagonal terms). In this author's mind, a solution preferable to those just mentioned is to employ one of the various "square root filters" which have been developed.

The basic idea behind square root filtering is to propagate and update an error covariance square root or inverse covariance square root rather than the covariance or its inverse themselves. The advantage of this approach, again quoting Maybeck, include the following

"The square root approach can yield twice the effective precision of the conventional filter in ill-conditioned problems. In other words, the same precision can be achieved with approximately half the wordlength. Moreover, this method is completely successful in maintaining the positive semidefiniteness of the error covariance." (Ref. 16:13)

Among the square root recursions that have been developed are the Potter covariance square root, Carlson covariance square root, inverse covariance square root, and the U-D covariance factorization. The reader is referred to Reference 16 for an excellent discussion of these four square root recursive algorithms.

The approach finally adopted for this problem was the U-D covariance factorization method. Although not strictly

a square root filter, the U-D covariance factorization filter is closely related and provides all of the numerical precision of the square root filters but without performing any time consuming square root operations. Actually, for this problem the U-D factorization was only used for the covariance and state estimate updating. Propagation of the state estimate and covariance between measurements was performed by numerically integrating eqns. (3-3) and (3-4) as discussed previously. This was done because it was felt that only during measurement updating was the numerical instability of the Kalman filter algorithm evidenced, and because U-D propagations depend on the linearity of the model. The U-D covariance factorization recursion for updating the state estimate and error covariance will now be given. No attempt is made to derive the equations but only to give the filter algorithm itself. For additional details and discussion see Reference 16, section 8. What follows was taken from this same source.

U-D Covariance Factorization Update (Ref. 16:42-47)

This method expresses the covariance before and after measurement updating as

$$\underline{P}^- = \underline{U}^- \underline{D}^- \underline{U}^{-T} \quad (3-24)$$

$$\underline{P}^+ = \underline{U}^+ \underline{D}^+ \underline{U}^{+T} \quad (3-25)$$

where \underline{U} matrices are upper triangular and unitary (i.e., ones along the diagonal) and the \underline{D} matrices are diagonal. As was stated previously, the U-D filter is not strictly speaking a square root filter, but it is considered such

because $\underline{U}\underline{D}^{\frac{1}{2}}$ corresponds directly to the covariance square root.

The algorithm as employed here begins at the end of the current time propagation interval (t_i), when $\underline{P}(t_i^-)$, a $n \times n$ symmetric, positive semidefinite matrix is returned by ODE. The first step, then, is to generate the \underline{U}^- and \underline{D}^- factors of \underline{P}^- . The following algorithm will generate a uniquely defined pair of U-D factors.

First, for the n -th column

$$\begin{aligned} D_{nn} &= P_{nn} \\ U_{in} &= \begin{cases} 1 & i=n \\ P_{in}/D_{nn} & i=n-1, n-2, \dots, 1 \end{cases} \end{aligned} \quad (3-26a)$$

Then for the remaining columns, for $j = n-1, n-2, \dots, 1$, compute:

$$\begin{aligned} D_{jj} &= P_{jj} - \sum_{k=j+1}^n D_{kk} U_{jk}^2 \\ U_{ij} &= \begin{cases} 0 & i > j \\ 1 & i = j \\ [P_{ij} - \sum_{k=j+1}^n D_{kk} U_{ik} U_{jk}] / D_{jj} & i = j-1, j-2, \dots, 1 \end{cases} \end{aligned} \quad (3-26b)$$

The matrices \underline{U}^- and \underline{D}^- have now been computed. The scalar measurement update for the U-D filter will now be given.

Using the measurement value z_j and the known $1 \times n$ $\underline{H}(t_i)$ and scalar $r(t_i)$, one computes

$$\left. \begin{aligned} \underline{f} &= \underline{U}^{-T} \underline{H}^T \\ v_j &= D_{jj}^{-1} f_j \\ a_0 &= r \end{aligned} \right\} \quad j = 1, 2, \dots, n \quad (3-27)$$

Then for $K = 1, 2, \dots, n$, one calculates

$$\begin{aligned}
 a_k &= a_{k-1} + f_k v_k \\
 D_{kk}^+ &= D_{kk}^- a_{k-1} / a_k \\
 b_k &\leftarrow v_k \\
 p_k &= -f_k / a_{k-1} \\
 U_{jk}^+ &= U_{jk}^- + b_j p_k \\
 b_j &\leftarrow b_j + U_{jk}^- v_k
 \end{aligned}
 \left. \vphantom{\begin{aligned} a_k \\ D_{kk}^+ \\ b_k \\ p_k \\ U_{jk}^+ \\ b_j \end{aligned}} \right\} \begin{array}{l} \\ \\ \\ \\ j=1, 2, \dots, (k-1) \end{array} \quad (3-28)$$

In eqn. (3-28), " \leftarrow " denotes replacement, or "writing over" old variables for efficiency. For $K=1$, only the first three equations are needed. After the n iterations of eqn. (3-28), \underline{U}^+ and \underline{D}^+ have been computed, and the filter gain $K(t_i)$ can be calculated in terms of the n -vector \underline{b} made up of components b_1, b_2, \dots, b_n computed in the last iteration of eqn. (3-28), and the state updated as

$$\begin{aligned}
 K(t_i) &= \underline{b} / a_n \\
 \hat{\underline{x}}(t_i^+) &= \hat{\underline{x}}(t_i^-) + K(t_i) [z_i - H(t_i) \hat{\underline{x}}(t_i^-)] \quad (3-29)
 \end{aligned}$$

Vector measurements updates for $\underline{R}(t_i)$ diagonal, as was the case here, are performed component by component.

The covariance update is computed by eqn. (3-25) and then ODE is called again to propagate the state and covariance ahead to the next measurement time (t_{i+1}) .

Before leaving this subject, a brief comparison owed to Maybeck (Ref. 16:54-57) will be given. Table III presents the number of operations required for one time propagation and one measurement update for the case of $n=10$, $s=10$, and $m=2$, where n is the state dimension, s is the noise dimension,

s is the noise dimension, and m is the measurement dimension. The last column of Table III gives the processor time for one filter cycle based on the following instruction times typical of the IBM 360:

addition = 2.7 μ sec
multiplication = 4.1 μ sec
division = 6.6 μ sec
square root = 60.0 μ sec

Table III. Operations for One Filter Cycle
(n=s=10, m=2)

Filter	ADDS	MULTIPLIES	DIVIDES	SQUARE ROOTS	TIME (MSEC)
Conventional Kalman	2340	2690	2	0	17.36
Joseph Form Kalman	3631	4498	3	0	28.27
U-D Factor	2935	3330	29	0	21.77

As Table III shows, for the case given, the U-D filter falls between the conventional Kalman filter and the Joseph form Kalman filter in processing time. However, for a modest increase in computational burden over the conventional Kalman filter one avoids its numerical instability and gains twice the accuracy in the same wordlength by employing the U-D filter. Based on Table III, one wonders why it would ever be advantageous to use the Joseph form over, say, the U-D covariance factorization.

The initial choice of the Joseph form for use in the

problem under study here was motivated by a desire for numerical accuracy. What was overlooked was the fact that numerical accuracy does not insure numerical stability.

Truth Model

The truth model for this problem consisted of a 4-state model of the system dynamics plus the 3 deterministic gravity disturbance states. The true state vector is given by,

$$\underline{X}_T = \begin{bmatrix} r \\ V_r \\ \omega_{\text{los}_y} \\ \omega_{\text{los}_z} \\ \delta g_x \\ \delta g_y \\ \delta g_z \end{bmatrix} = \begin{bmatrix} X_1 \\ X_2 \\ X_3 \\ X_4 \\ \delta g_x \\ \delta g_y \\ \delta g_z \end{bmatrix} \quad (3-30)$$

and the state differential equations are

$$\dot{\underline{X}}_T = \begin{bmatrix} \dot{X}_1 \\ \dot{X}_2 \\ \dot{X}_3 \\ \dot{X}_4 \end{bmatrix} = \begin{bmatrix} X_2 \\ X_1 (X_3^2 + X_4^2) + \delta g_x \\ (-2X_2X_3 - \delta g_z)/X_1 \\ (-2X_2X_4 + \delta g_y)/X_1 \end{bmatrix} \quad (3-31)$$

In the truth model, perfect tracking was assumed, and thus, $\delta\eta$ and $\delta\epsilon$ are zero for all time. This assumption was made since the tracking loop would typically be operating with a much lower period than the filter cycle time of 10 sec. In view of this it was decided not to model tracker dynamics. In any further work in this area, a shorter filter cycle could be used and a dynamic model of the tracker added to the

truth model.

The δg components were determined by running the program GTGRV discussed in Reference 25. Inputs to GTGRV were data cards with the positions (expressed in e-frame coordinates) at which the gravity vector \underline{g} and gradient matrix $\underline{\Gamma}$ were desired. Formulas used by GTGRV to calculate the gravity vector and gradient contributions of each point mass in the gravity field are given in Reference 25, Appendix B, pp. 5-7. Seven point-mass sets were used in the calculations with grid sizes of 5° , 1° , $15'$, $5'$, $2.5'$, $1.25'$, and $0.3125'$, where "(o)" means degree of longitude and latitude and "(')" means minute of longitude and latitude ($60' = 1^\circ$). The outputs of GTGRV used in this study were the δg and Γ_{xx} , Γ_{xy} , and Γ_{xz} components expressed in e-frame coordinates.

The "true" state vector, \underline{x}_T , was obtained by direct numerical integration of the differential equations in eqn. (3-31) using the δg components calculated by GTGRV. There were no noise inputs to the state dynamics.

Gravity Gradient Estimate

The gravity gradient $\underline{\Gamma}$ as discussed in Appendix A can be written as

$$\underline{\Gamma} = \frac{\partial \underline{g}}{\partial \underline{r}} \quad (3-32)$$

where, \underline{g} is the gravity vector as a function of position, \underline{r} , and to first order,

$$\left[\frac{\partial \underline{g}}{\partial \underline{r}} \right] \approx \left[\frac{\delta \hat{\underline{g}}}{\delta \underline{r}} \right] = \begin{bmatrix} \frac{\delta \hat{g}_x}{\delta r_x} & \frac{\delta \hat{g}_x}{\delta r_y} & \frac{\delta \hat{g}_x}{\delta r_z} \\ \frac{\delta \hat{g}_y}{\delta r_x} & \frac{\delta \hat{g}_y}{\delta r_y} & \frac{\delta \hat{g}_y}{\delta r_z} \\ \frac{\delta \hat{g}_z}{\delta r_x} & \frac{\delta \hat{g}_z}{\delta r_y} & \frac{\delta \hat{g}_z}{\delta r_z} \end{bmatrix} \quad (2-10)$$

Obviously, the accuracy with which one can approximate

the gradient with this technique is directly proportional to the accuracy of the $\delta\hat{g}$ estimate. Likewise, one would expect a better approximation to the true Γ for $|r|$ small. Of course, as $|r|$ decreases so does $|\delta g(r)|$, which poses prob- for the EKF estimator in view of the noise process strengths.

Figures 17 and 18 show plots of the true Γ_{xx} , Γ_{xy} , and Γ_{xz} components for both altitude cases simulated. Notice that the true Γ values are in the range of several tens of EU (Eötvös Units = 10^{-9}sec^{-2}). In this simulation, only a tracker-target pair along the x_e -axis was used. Thus, the components estimated by eqn. (2-10) for this problem are Γ_{xx} , Γ_{xy} , and Γ_{xz} , or the first column of the Γ matrix. With one pair of trackers and targets one gets three of the five independent elements of Γ . One additional pair ortho- gonal to the first pair, say, along the y_e -axis would provide the other two independent elements and the entire gravity gradient tensor would be determined. In practice, a third pair along the z_e -axis would probably be desirable so that data smoothing could be exploited to hopefully improve the estimate of Γ .

The added components in the full-up system instrumenting all three axes would not increase the state vector dimension by a factor of three. Instead, the additional two axes would add two range states, two range rate states, one ω_{LOS} state and one angular deviation state.

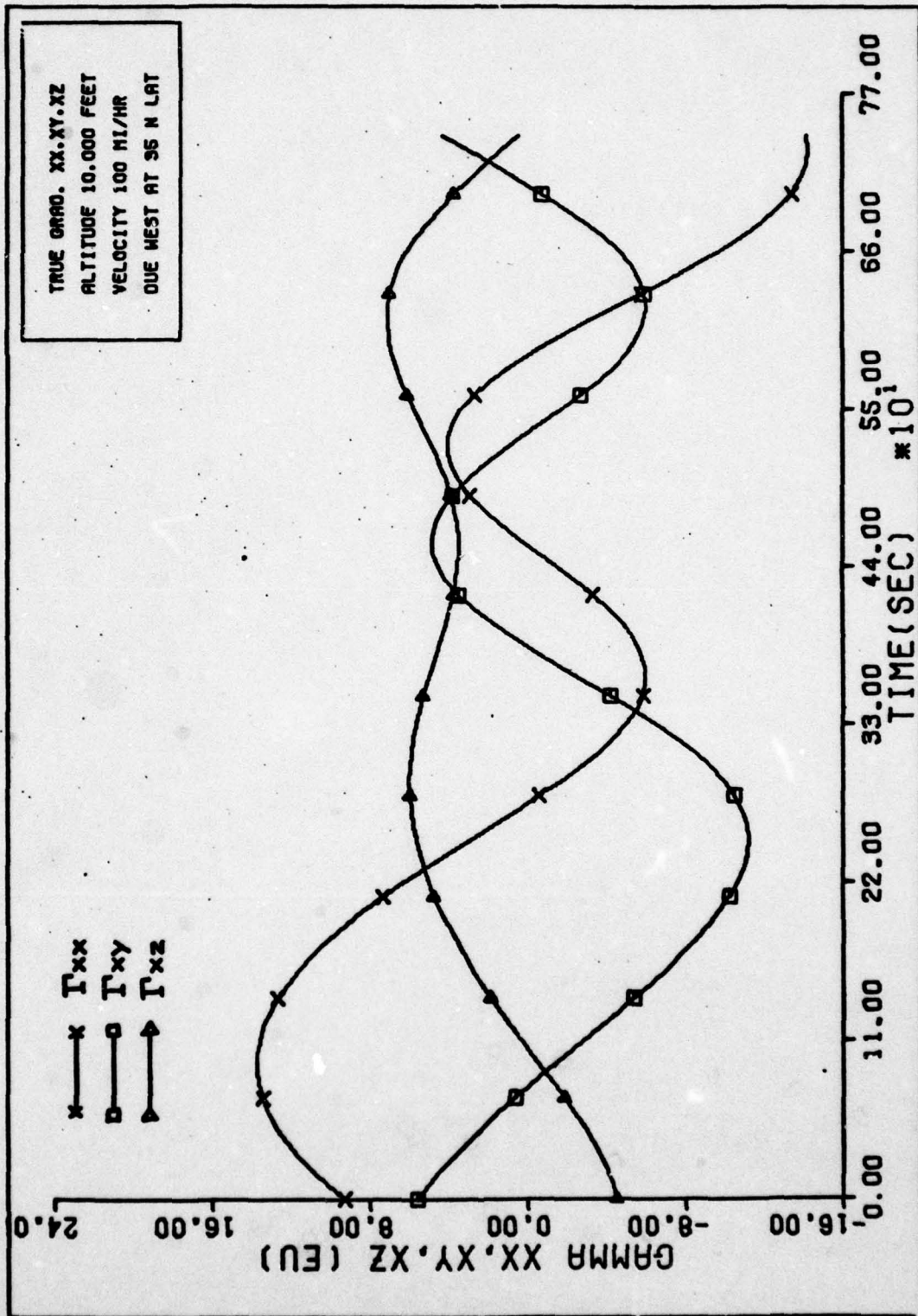


FIG. 17 TRUE GRADIENTS Γ_{xx} , Γ_{xy} , AND Γ_{xz} . (10,000 feet)

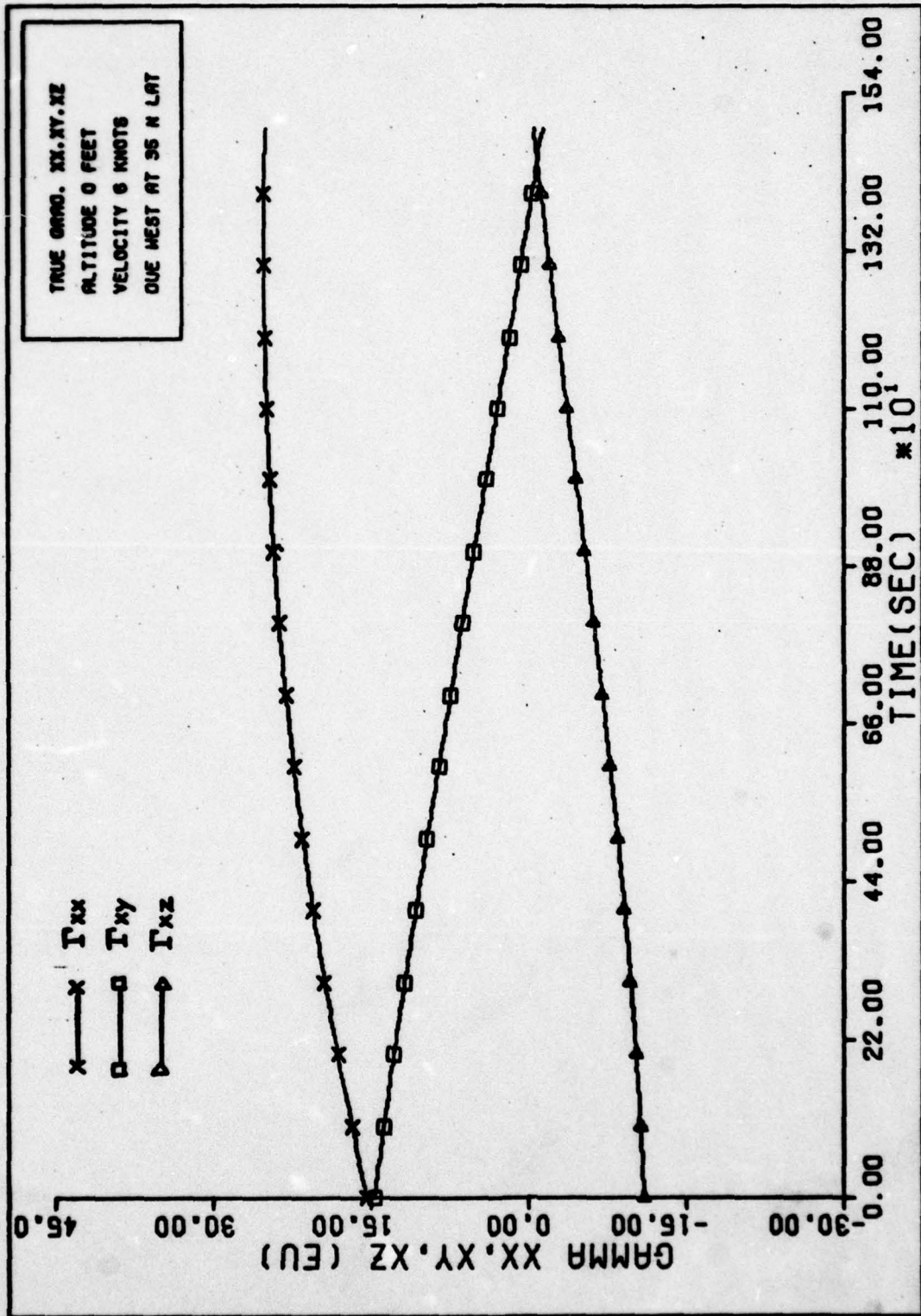


FIG. 18 TRUE GRADIENTS Γ_{xx} , Γ_{xy} , AND Γ_{xz} . (0 feet)

IV. Monte Carlo Analysis and Results

Monte Carlo Method

The Monte Carlo study is one of two fundamental techniques of conducting a performance (sensitivity) analysis of a prospective Kalman filter. One seeks an accurate statistical portrayal of the filter's estimation errors without having to build the filter and test it in a "real world" environment. One can do this via computer simulation wherein the "real world" is replaced by a truth model, the most complete mathematical model one can devise to simulate the real world.

Figure 19 illustrates how a performance analysis of a Kalman Filter might be conducted. This figure does not represent the most general performance evaluation mechanization but is tailored to the needs of the problem under study.

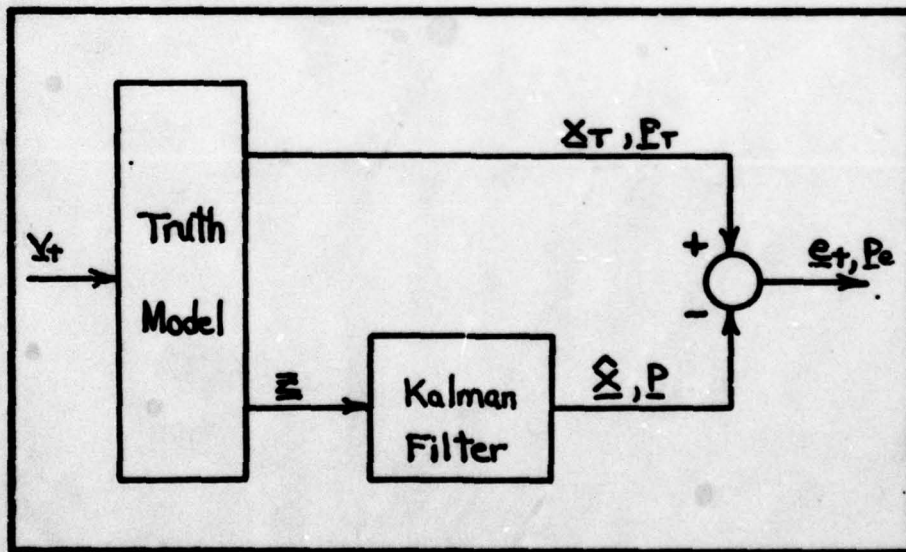


Fig. 19 Performance Evaluation of a Kalman Filter

From the truth model, the true state vector, \underline{x}_T , and the true covariance, \underline{P}_T , are generated. The white Gaussian noise process, \underline{v}_T , drives the truth model to accurately generate the measurements, \underline{z} . The Kalman filter combines the measurement information with its own internal dynamics model of the system and produces its own "best" estimate of the states, $\hat{\underline{x}}$, and covariance, \underline{P} . The error process, \underline{e}_T , and error covariance, \underline{P}_e , are formed by the "difference" between the true states and the filter states. This "difference" must be modified from its accepted meaning to account for the differences in dimension between the truth model and filter model in the general case. The objective of the performance analysis is to statistically characterize, \underline{e}_T .

Already mentioned as a technique for generating the statistics of \underline{e}_T is the Monte Carlo study. The other widely used technique is a mean and covariance analysis. This technique is exploited when the truth model is a linear system driven by white Gaussian noise and having linear measurements corrupted by white Gaussian noise. Since a non-linear system is involved in this study, the covariance analysis is not used and will not be discussed further.

In conducting a Monte Carlo study, many samples of \underline{e}_T are generated by simulation, and the ensemble average, or statistical behavior of \underline{e}_T is computed directly. Theoretically, an infinite number of simulations is necessary to insure that the computed sample statistics do, in fact, portray the filter's performance. Obviously, conducting an infinite

number of simulations is out of the question, so only a limited number of simulations are conducted. Choosing the number of simulations which will result in process statistics which adequately reflect the "true" statistics is often influenced by the need to conserve computer time and stay within budget constraints. Although there are no rules which govern the choosing of an appropriate number of simulations, the degree of non-linearity in the truth model is certainly a factor. For problems with insignificant non-linearities and modest state dynamics perhaps as few as 5-10 simulations would suffice. On the other hand, for highly non-linear models as many as 15-25 simulations (or more) may be desirable. Again, time and budget constraints may well dictate an upper limit, but one should be wary of drawing conclusions about filter performance based on inadequate statistics.

One means of choosing an appropriate number of simulations is to plot each states' changes in computed variance versus the number of simulations. Such a plot will typically reach nearly steady state conditions where adding more simulations does little to the sample statistics. An appropriate number of simulations can then be chosen from the steady state region.

The Monte Carlo analysis was never completed in this case because of severe numerical problems encountered during the simulations. These problems are discussed next.

Results

The Monte Carlo analysis was never successfully

completed; and, consequently, few results can be reported. From the beginning of the start of simulation runs, the EKF exhibited divergence. Within two or three filter cycles, the \underline{P} matrix would lose positive semidefiniteness and the state estimates would begin to grow, seemingly without bound. Many attempts were made to correct the problem.

The first attempt was to try to tune the filter. Tuning a Kalman Filter involves adjusting the \underline{P}_0 , $\underline{Q}(t)$, and $\underline{R}(T_i)$ values to obtain the "best" performance possible. Many tuning runs were made but to no avail.

This problem was known to be ill-conditioned numerically because of the wide range of values between state variables (range was on the order of 10m while δg components got as small as 10^{-8} m/sec²). The decision to change the form of the filter update equations was based on a desire to exploit the superior numerical characteristics of the U-D covariance factorization update algorithm. When this change was made, loss of positive semidefiniteness of \underline{P} was still observed although it did not occur until the third or fourth filter cycle.

Once again many tuning runs were made but without alleviating the problem. It was assumed, at this point, that the numerical ill-conditioning of the problem was at the heart of the filter instability.

With time running out, a final attempt was made to scale the variables. This was done by scaling each variable to fall in the range of $0 < x \leq 2$.

The formula used for scaling was

$$Y = \frac{X - X_{\min}}{\left(\frac{X_{\max} - X_{\min}}{2}\right)} \quad (4-1)$$

where:

X = old variable,

Y = scaled variable.

X_{\max} = maximum value of X based on the truth model data, and

X_{\min} = minimum value of X based on the truth model data.

After scaling, several tuning runs were conducted. It was discovered that only by increasing the values for the elements of $\underline{R}(t_i)$ (i.e., increasing the uncertainty in the measurements) could positive semidefiniteness in \underline{P} be maintained. The original $\underline{R}(t_i)$ was given by

$$\underline{R}(t_i) = \begin{bmatrix} 10^{-10} & 0 & 0 \\ 0 & 10^{-12} & 0 \\ 0 & 0 & 10^{-12} \end{bmatrix} \quad (4-2)$$

while the $\underline{R}(t_i)$ for the only case where the filter worked successfully was

$$\underline{R}(t_i) = \begin{bmatrix} 10^{-6} & 0 & 0 \\ 0 & 10^{-7} & 0 \\ 0 & 0 & 10^{-7} \end{bmatrix} \quad (4-3)$$

The inability of the filter to avoid numerical instability even after scaling and the U-D covariance update were implemented was entirely unexpected. The explanation lies in the small eigenvalues of $\underline{R}(t_i)$ as originally proposed. Measurements of this accuracy appear to the filter to be nearly perfect, and this leads to numerical instability in the Kalman filter algorithm. This indicates that perhaps the EKF was a poor choice of estimator to employ in this problem and leads to a number of recommendations to be covered in Chapter V.

V. Conclusions and Recommendations

Conclusions

As has already been stated, the lack of positive results in this study, although disappointing in the extreme, does not invalidate the proposal advanced in this thesis. Rather, it has been shown that the problem is extremely ill-conditioned and the Extended Kalman Filter is not an appropriate choice for this application. As a result of the effort expended in the course of this study, the following have been achieved:

- (1) A proposal has been made for an alternative approach to gravity gradient estimation.
- (2) The state equations upon which to base an estimator have been developed.
- (3) This study delineated some of the numerical problems which any subsequent work in this area must address. Some tentative solutions were explored without significant improvement in the results.
- (4) The Extended Kalman Filter has been shown to be a poor choice for this application.
- (5) The method of gravity gradient estimation proposed here should probably be restricted to use in a ship or submarine environment.

Recommendations

First, a plea must be made for someone to continue the investigation started here. The proposal deserves an adequate test of its feasibility.

The numerical problems encountered in this study should be a lesson for anyone attempting a similar study. The

problem posed here is extremely ill-conditioned. The failure of scaling and the U-D Covariance factorization update to solve the numerical instability problem testifies to this fact.

The simple EKF chosen for implementation was unable to cope with this problem. Alternative approaches which might be more fruitful include employing higher order nonlinear filters such as Modified Gaussian second-order or Modified Truncated second-order filters.

A different approach altogether such as using batch processing of the data in an off-line analysis by maximum likelihood techniques might also prove attractive. There are several approaches which might be considered, but this study does not clearly indicate which would provide the best performance.

With regard to the differential gravity disturbance modelling issue, this is one area in which much more effort is needed. If the assumption that the point-mass gravity model used here adequately represents the anomalous field is valid, then a detailed time series analysis of the spectral characteristics of this field would be useful. From such an analysis, better stochastic models for the differential differential disturbance components could be obtained.

Two other issues which need to be addressed include an analysis of the optimum spacing of the target and tracker for best gradient estimation and a study of how the concept of repeating the same flight profile could be used to improve

the gradient estimate.

Finally, the extension of this study to a full three axis implementation would be valuable in ascertaining the practical limits to the gradient estimation accuracies that could be achieved by this technique. The potential future benefits of more research in this area include better knowledge of the earth's gravity field and subsequent improvements in aerospace and seaborne vehicle navigation and guidance.

Bibliography

1. Bate, Roger R., et al. Fundamentals of Astrodynamics. New York: Dover Publications, Inc., 1971.
2. Britting, Kenneth R. Inertial Navigation Systems Analysis. New York: Wiley-Interscience, a division of John Wiley and Sons, Inc., 1971.
3. Comfort, Gary C. A Study of Airborne Gravimetry Using Repeated Flight Paths. Report. U.S. Air Force Academy, Colorado: Frank J. Seiler Research Laboratory, August 1974. (AD-A003498).
4. Edwards, Robert M. Gravity Modeling for Precise Terrestrial Inertial Navigation. Dissertation prospectus. Wright-Patterson AFB, Ohio: Air Force Institute of Technology, June 1977. (AD-A042419).
5. Frey, Elmer J. and Raymond B. Harlan. "Application of Inertial Technology to Airborne Gravimetry," NATO AGARD Conference Proceedings No. 43, May 1968. (AD-692540).
6. Gelb, Arthur (editor). Applied Optimal Estimation. Cambridge, Mass.: MIT Press, 1974.
7. Halliday, David and Robert Resnick. Physics, Part II. New York: John Wiley and Sons, Inc., 1962.
8. Hand, James and John DiSorbo. Advanced Concept for Inertial Navigator Updates. Technical report C-4453. Cambridge, Mass.: The C.S. Draper Laboratories, Inc., revised December 1975.
9. Harris, R.A., et al. Coordinate System Alignment Technology Final Task Report. Technical report R-1023. Cambridge, Mass.: The Charles Stark Draper Laboratory, Inc., December 1976.
10. Heiskanen, W.A. and Helmut Moritz. Physical Geodesy. San Francisco: W.H. Freeman and Co., 1967.
11. Heller, Warren G. Models for Aided Inertial Navigation System Sensor Errors. Technical report TR-312-3. Reading, Mass.: The Analytic Sciences Corp., February 8, 1975.
12. Karamcheti, K. Vector Analysis and Cartesian Tensors. San Francisco: Holden-Day, Inc., 1967.
13. Kasper, Joseph F., Jr. "A Second-Order Markov Gravity Anomaly Model," Journal of Geophysical Research, Vol. 76, No. 32, November 1971.

14. Kriegsman, Bernard A. and Keven B. Mahar. Anomalous-Gravity Estimation and Long-Term Submarine Navigation Using Gradiometers and an INS. Technical report 1204. Cambridge, Mass.: Charles Stark Draper Laboratories, August 1978.
15. Maybeck, Peter S. Stochastic Estimation and Control Systems. Class notes for EE 7.65, EE 7.66, and EE 7.68, Stochastic Estimation and Control I, II, III. School of Engineering, Air Force Institute of Technology, Wright-Patterson AFB, Ohio: to be published by Academic Press in 1979.
16. ----- Solutions to the Kalman Filter Wordlength Problem: Square Root and U-D Covariance Factorizations. Technical report AFIT-TR-77-6. Wright-Patterson AFB, Ohio: Air Force Institute of Technology, September 1977.
17. Metzger, Ernest H. and Albert Jircitano. "Analysis of Real Time Mapping of Horizontal and Vertical Gravity Anomalies Aboard a Moving Vehicle Such as an Aircraft," International Symposium on Applications of Marine Geodesy. Columbus, Ohio, June 1974.
18. Mitchell, Robert A.K. High Accuracy Aircraft to Satellite Tracking Using an Extended Kalman Filter. Masters thesis. Wright-Patterson AFB, Ohio: Air Force Institute of Technology, December 1974. (AD-A008716).
19. Musick, Stanton H. Geodetic Error Models for Simulating and Estimating INS Error Behavior. Technical memorandum, AFAL-TM-77-44. Wright-Patterson AFB, Ohio: Air Force Avionics Laboratory, September 1977.
20. Nikolai, Paul J. and Donald S. Clemm. Solution of Ordinary Differential Equations on the CDC 6600/CYBER 74 Processors. Technical memorandum, AFFDL-TM-76-130-FBR. Wright-Patterson AFB, Ohio: Air Force Flight Dynamics Laboratory, January 1977.
21. Papoulis, A. Probability, Random Variables, and Stochastic Processes. New York: McGraw-Hill Book Co., 1965.
22. Richman, Jack. Use of Multiple Sensors to Reduce Inertial Navigation Errors Caused by Gravitational Uncertainty. Report, KD-76-106. Little Falls, N.J.: Singer Kearfott Division, revision B, November 4, 1976.
23. ----- Reduction of Gravitation-Uncertainty Errors in Velocity-Damped Inertial Navigation Systems by Use of Multiple Platforms. Report, KD-77-12. Little Falls, N.J.: Singer Kearfott Division, February 15, 1977.

24. Slater, J.M. Inertial Guidance Sensors. New York: Reinhold Publishing Corp., 1964.
25. Smart, Richard W. Spherical Harmonic and Point-Mass Gravity Model Program. Report written for EE 6.39, Astronautical Guidance Laboratory. School of Engineering, Air Force Institute of Technology, Wright-Patterson AFB, Ohio, August 1978.
26. Widnall, William S. and Peter A. Grundy. Inertial Navigation System Error Models. Technical report TR-03-73. Cambridge, Mass.: Intermetrics, 11 May 1973. (AD-912489L).

Appendix A

The Gravity Gradient Tensor

A great deal of research is being conducted today on a new class of inertial instruments, gradiometers, whose purpose is to measure elements of the gravity gradient matrix. The system studied elsewhere in this report is another related approach to accomplish the same objective. What follows is a brief discussion of the mathematical properties of the gravity gradient tensor.

It is well known that gravitational potential is a scalar function ϕ of position \mathbf{r} relative to the attracting body (see for example Reference 10). The gravitational acceleration $\mathbf{g}(\mathbf{r})$ is the spatial derivative, or gradient, of the gravitational potential function. Expressed in Cartesian coordinates,

$$[\mathbf{g}(\mathbf{r})]^T = \begin{bmatrix} \frac{\partial \phi}{\partial x} & \frac{\partial \phi}{\partial y} & \frac{\partial \phi}{\partial z} \end{bmatrix} \quad (\text{A-1})$$

The gravity gradient tensor $\nabla \mathbf{g}(\mathbf{r})$, then, is the spatial derivative of $\mathbf{g}(\mathbf{r})$. Expressed in Cartesian coordinates,

$$[\nabla \mathbf{g}(\mathbf{r})] = \begin{bmatrix} \frac{\partial^2 \phi}{\partial x^2} & \frac{\partial^2 \phi}{\partial x \partial y} & \frac{\partial^2 \phi}{\partial x \partial z} \\ \frac{\partial^2 \phi}{\partial y \partial x} & \frac{\partial^2 \phi}{\partial y^2} & \frac{\partial^2 \phi}{\partial y \partial z} \\ \frac{\partial^2 \phi}{\partial z \partial x} & \frac{\partial^2 \phi}{\partial z \partial y} & \frac{\partial^2 \phi}{\partial z^2} \end{bmatrix} \quad (\text{A-2})$$

Since the gravity field is conservative, we have from Reference 12,

$$\nabla \times \mathbf{g} = 0 \quad (\text{A-3})$$

$$\nabla \cdot \mathbf{g} = 0 \quad (\text{A-4})$$

Equation A-3 expresses gravity gradient tensor symmetry and equation A-4, known as Laplace's equation, requires the trace of the gradient matrix to be equal to zero. These two considerations reduce the number of independent elements of the gradient matrix to five. Thus, complete determination of the tensor at any point requires five independent measurements.

In keeping with convention, the symbol Γ is used to represent the gravity gradient tensor,

$$[\Gamma] = \begin{bmatrix} \Gamma_{xx} & \Gamma_{xy} & \Gamma_{xz} \\ \Gamma_{xy} & \Gamma_{yy} & \Gamma_{zy} \\ \Gamma_{xz} & \Gamma_{zy} & \Gamma_{zz} \end{bmatrix} \quad (\text{A-5})$$

Appendix C

PSD Plots for Disturbance Data

The following six plots were obtained from the 150 data points representing the true gravity differential disturbance data. The IMSL library subroutine FTFREQ was used to compute the power spectra for plotting on the CALCOMP plotter.

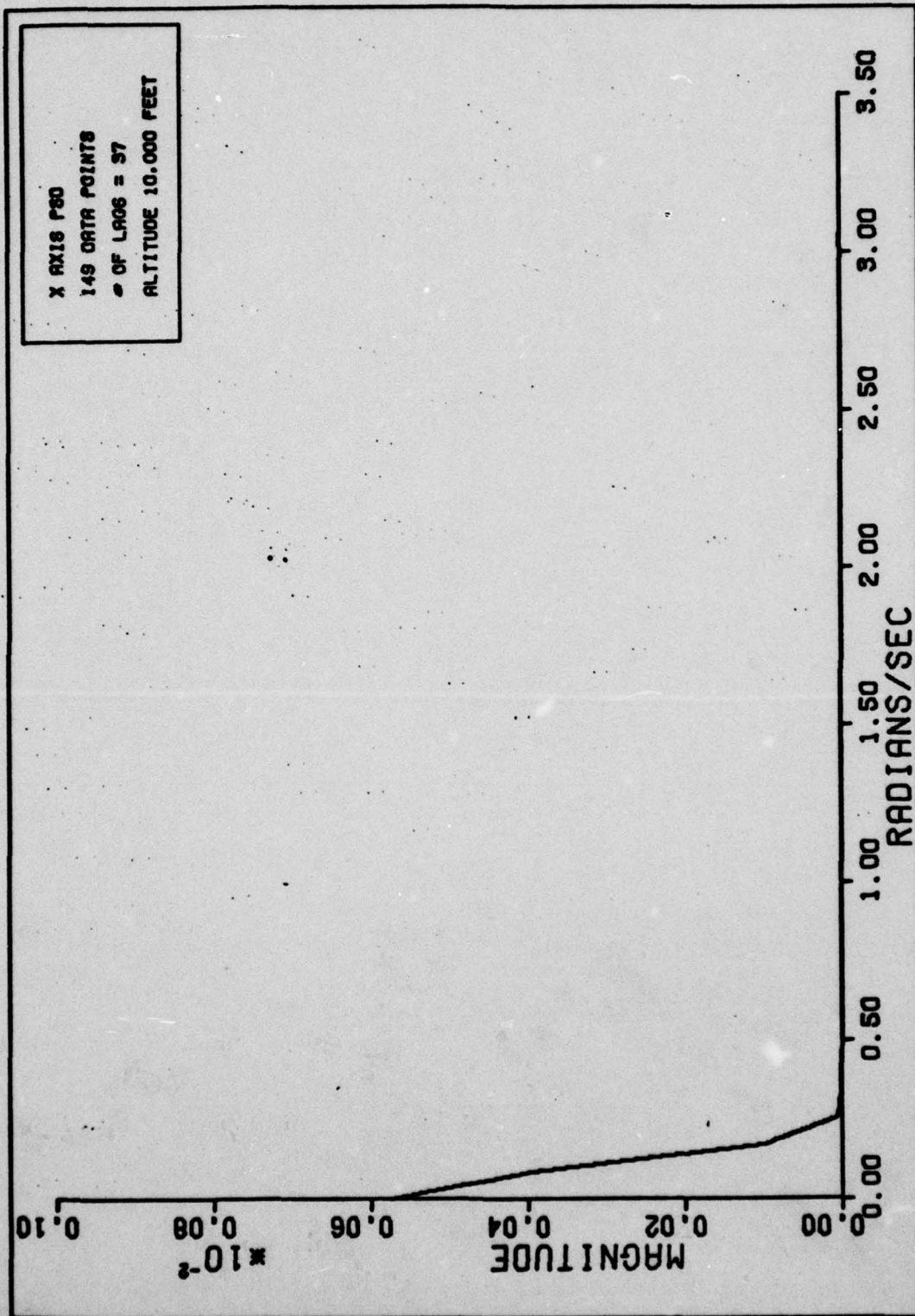


Fig. 20 PSD Plot of Delta G_x (10,000 ft.)

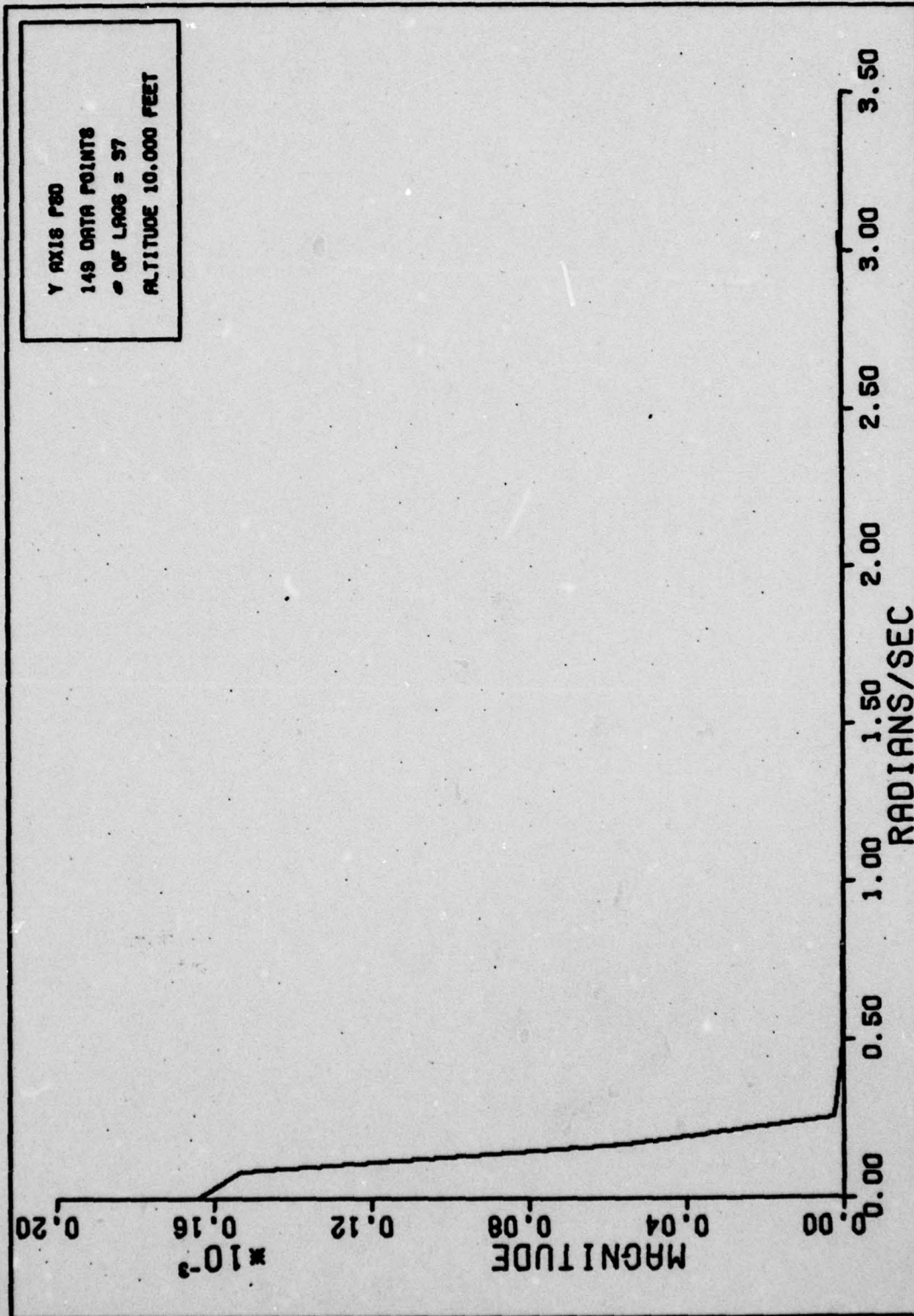


Fig. 21 PSD Plot of Delta G_y (10,000 ft.)

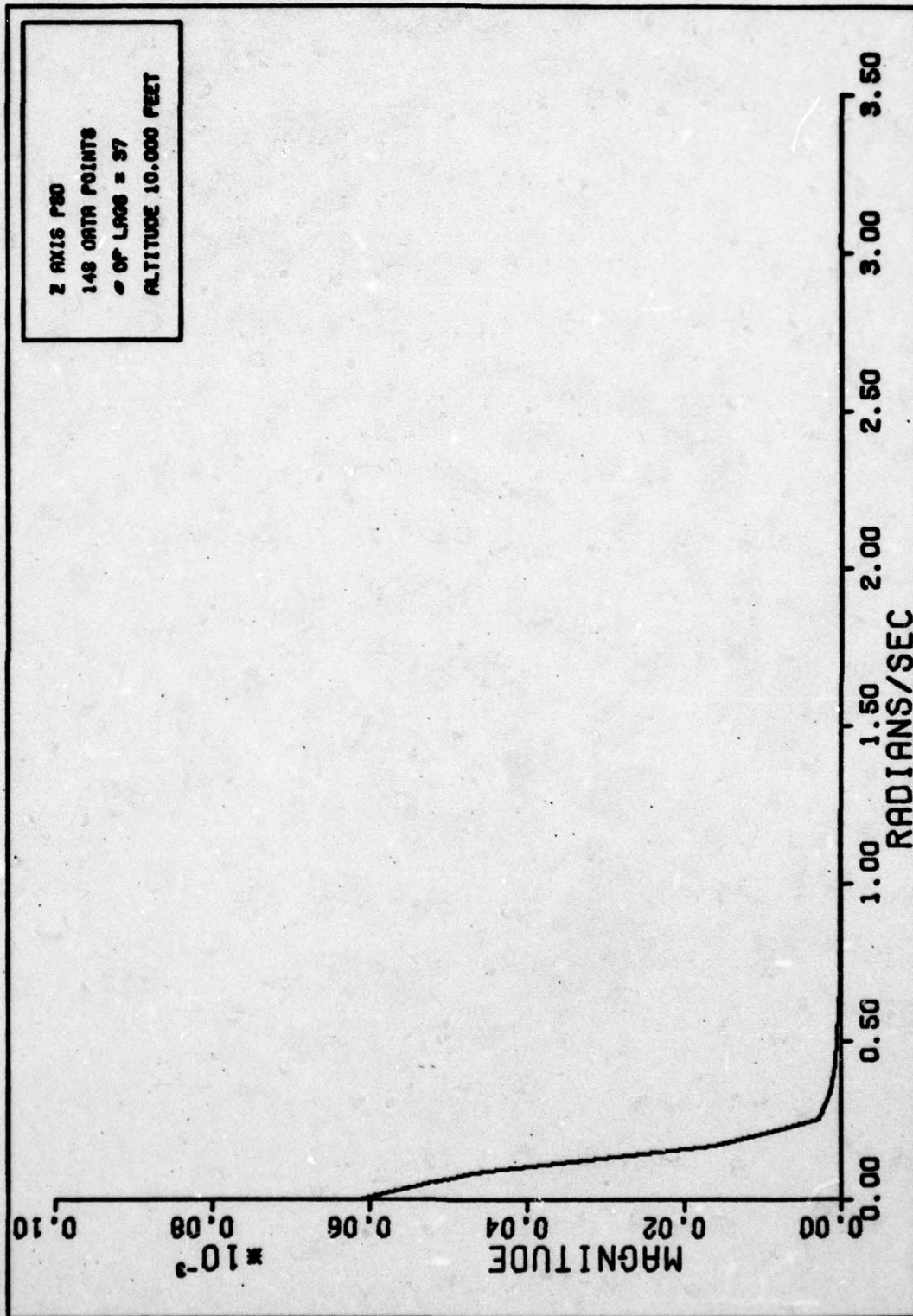


Fig. 22 PSD Plot of Delta G_z (10,000 Ft.)

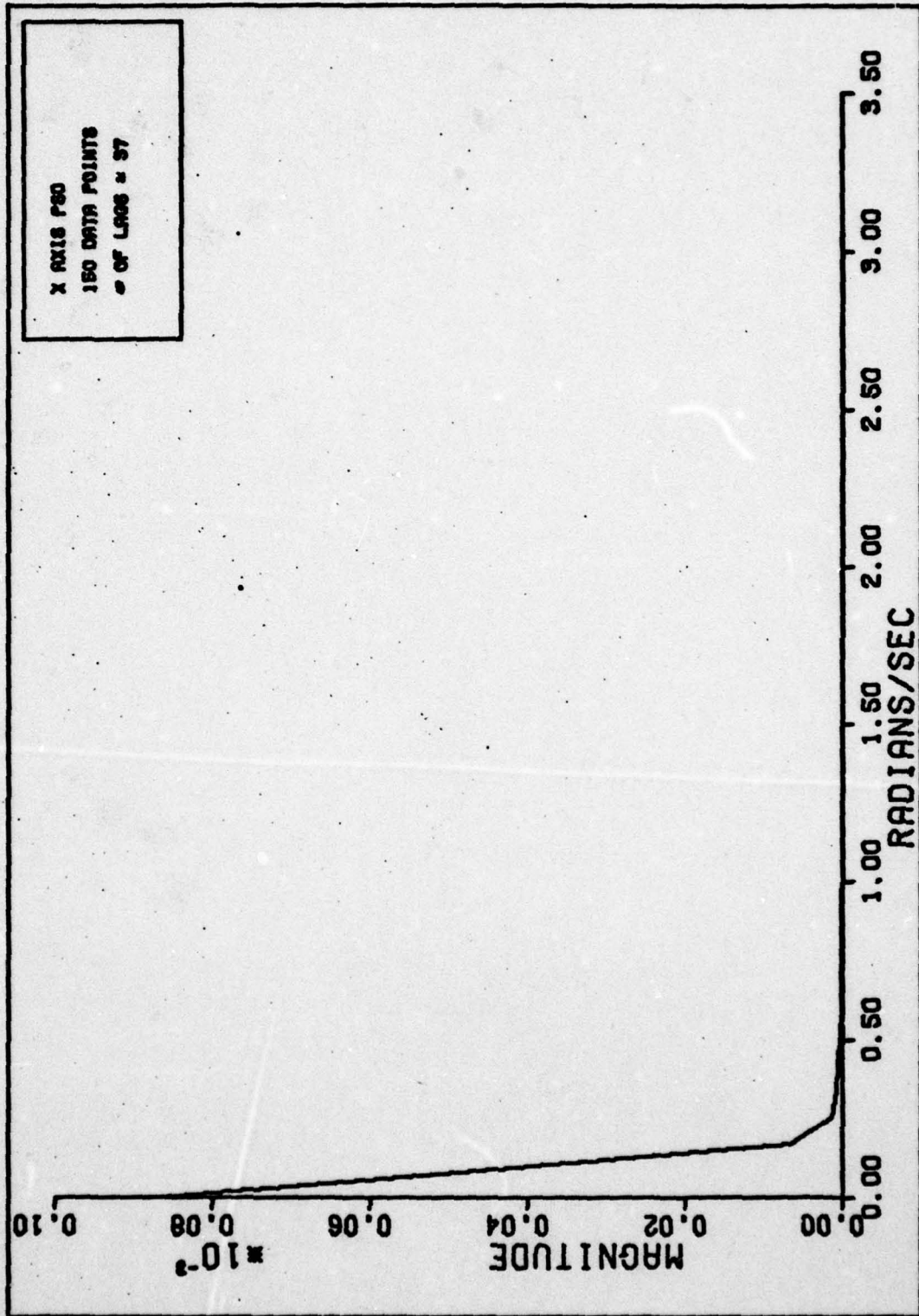


Fig. 23 PSD Plot of Delta G_x (0 ft.)

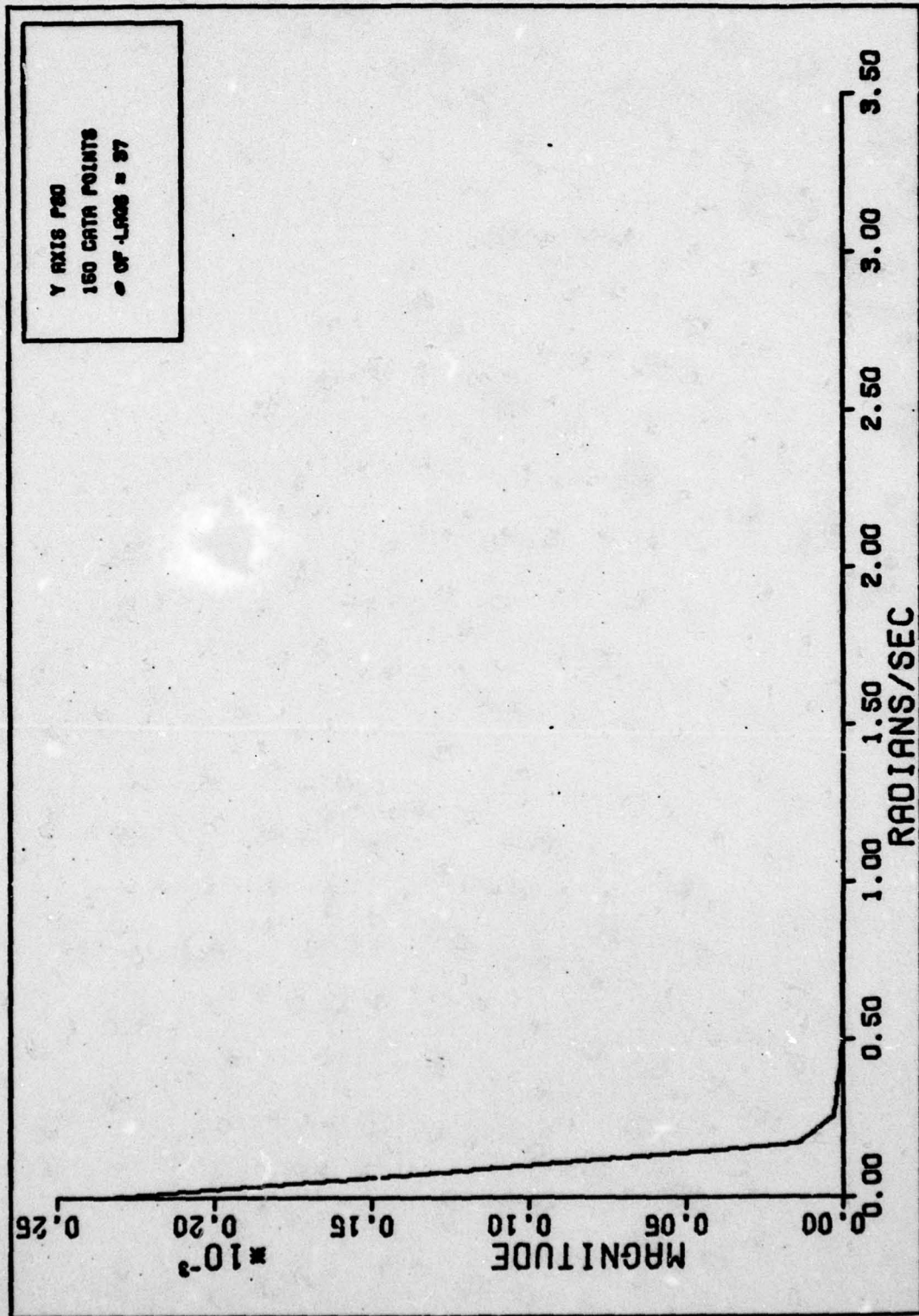


Fig. 24 PSD Plot of Delta C_y (0 ft.)

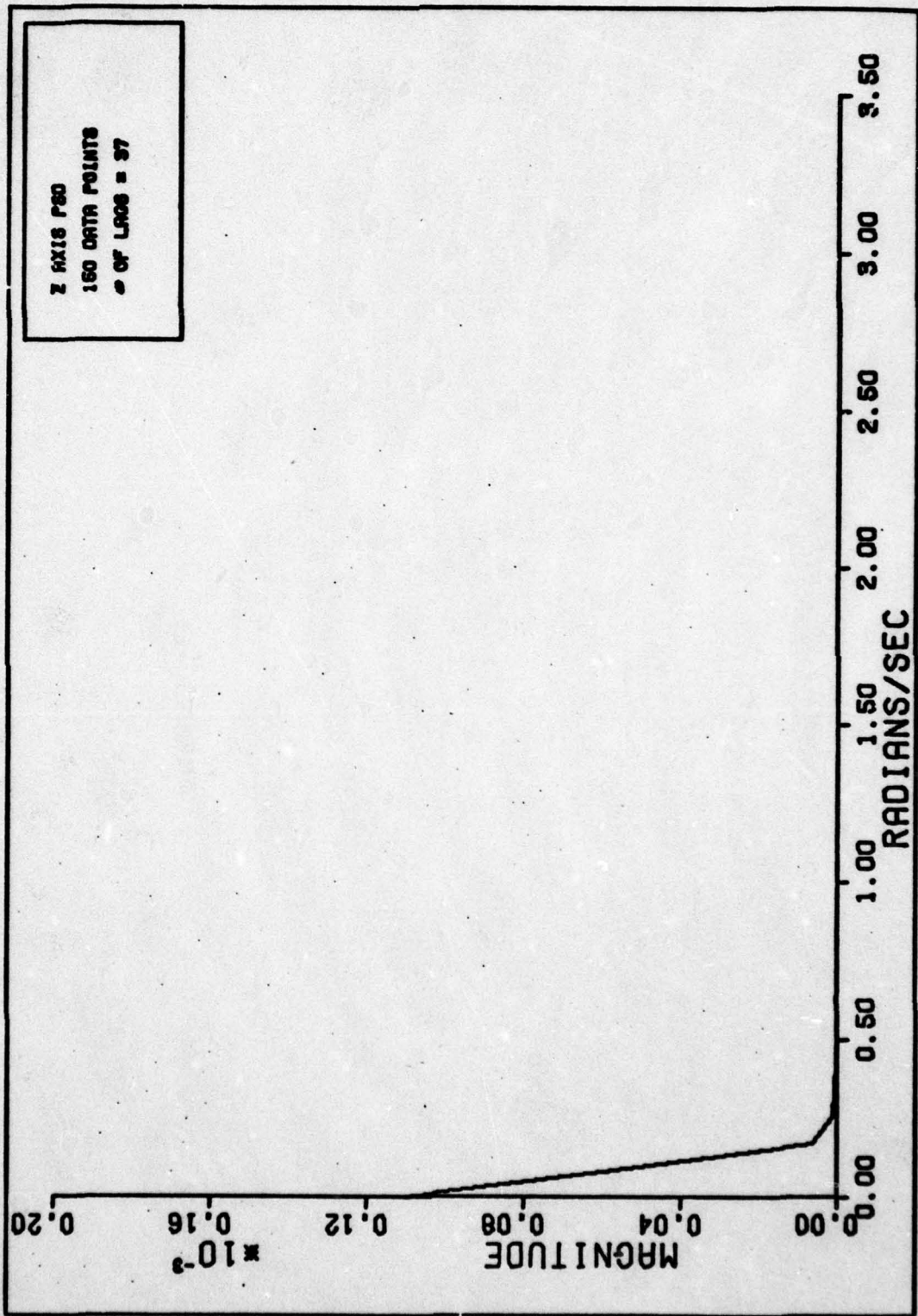


Fig. 25 PSD Plot of Delta G_z (0 ft.)

VITA

Richard Wayne Smart was born on 28 December 1946 at Ft. Bragg, North Carolina. He graduated from high school in Tacoma, Washington in 1964. In 1968 he enlisted in the USAF, and in 1969 he was selected for the Airman Education and Commissioning Program. He attended Auburn University from which he received the degree of Bachelor of Electrical Engineering in March 1971. After receiving his commission from OTS in June 1971, he served as a Satellite Operations Controller with the 6596 Instrumentation Squadron, Vandenberg AFB, California and as Chief, Satellite Operations Team for the Satellite Data System Program, Det 1 AFSCF, Sunnyvale AFS, California. In June 1977 he entered the School of Engineering, Air Force Institute of Technology.

Permanent address: 2898 Redditt Rd.
Orlando, Florida 32807

Unclassified

SECURITY CLASSIFICATION OF THIS PAGE (When Data Entered)

REPORT DOCUMENTATION PAGE		READ INSTRUCTIONS BEFORE COMPLETING FORM
1. REPORT NUMBER AFIT/GGC/EE/79-3	2. GOVT ACCESSION NO.	3. RECIPIENT'S CATALOG NUMBER
4. TITLE (and Subtitle) ESTIMATION OF THE ANOMALOUS GRAVITY GRADIENT VIA PRECISION ANGLE TRACKING		5. TYPE OF REPORT & PERIOD COVERED MS Thesis
		6. PERFORMING ORG. REPORT NUMBER
7. AUTHOR(s) Richard W. Smart Captain USAF		8. CONTRACT OR GRANT NUMBER(s)
9. PERFORMING ORGANIZATION NAME AND ADDRESS Air Force Institute of Technology (AFIT-EN) Wright-Patterson AFB, Ohio 45433		10. PROGRAM ELEMENT, PROJECT, TASK AREA & WORK UNIT NUMBERS
11. CONTROLLING OFFICE NAME AND ADDRESS Air Force Avionics Laboratory/RWA Wright-Patterson AFB OH 45433		12. REPORT DATE December 1978
		13. NUMBER OF PAGES 96
14. MONITORING AGENCY NAME & ADDRESS (if different from Controlling Office)		15. SECURITY CLASS. (of this report) Unclassified
		15a. DECLASSIFICATION/DOWNGRADING SCHEDULE
16. DISTRIBUTION STATEMENT (of this Report) Approved for public release; distribution unlimited.		
17. DISTRIBUTION STATEMENT (of the abstract entered in Block 20, if different from Report)		
18. SUPPLEMENTARY NOTES Approved for public release; IAW AFR 190-17 Joseph P. Hipps, Major, USAF Director of Information 16 MAY 1979		
19. KEY WORDS (Continue on reverse side if necessary and identify by block number) Gravity Gradient Extended Kalman Filter U-D Covariance Factorization Tracking		
20. ABSTRACT (Continue on reverse side if necessary and identify by block number) A preliminary feasibility study was done on a proposal to estimate the anomalous gravity gradient via precision measurements between two accelerometer triads moving through a gravity field. The state equations to describe the system were developed and an Extended Kalman Filter was designed to exploit the measurement data. A simple, first-order numerical approximation was used in gradient estimation. In addition, a brief → next page		

DD FORM 1473 1 JAN 73

EDITION OF 1 NOV 65 IS OBSOLETE

Unclassified

SECURITY CLASSIFICATION OF THIS PAGE (When Data Entered)

AD-A069 209

AIR FORCE INST OF TECH WRIGHT-PATTERSON AFB OHIO SCH--ETC F/G 17/7
ESTIMATION OF THE ANOMALOUS GRAVITY GRADIENT VIA PRECISION ANGL--ETC(U)
DEC 78 R W SMART

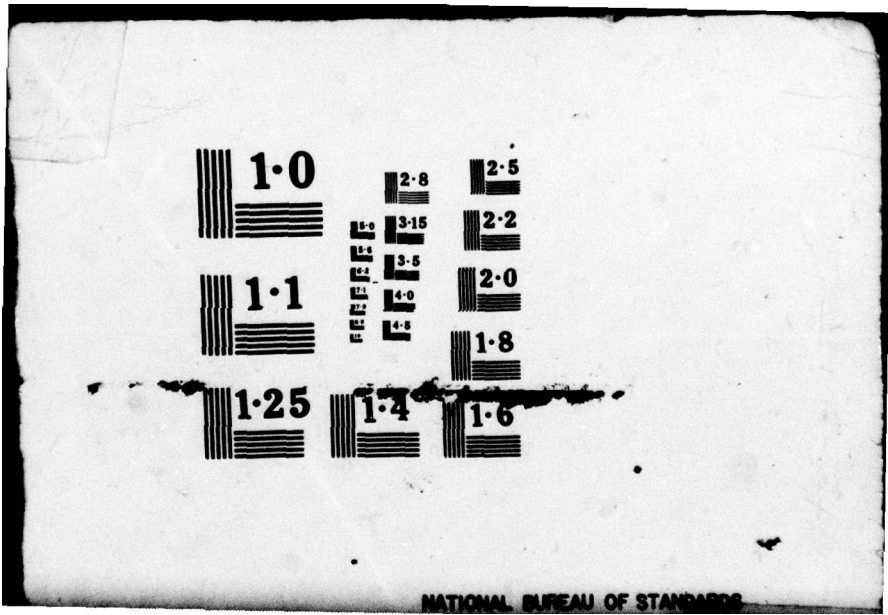
UNCLASSIFIED

AFIT/G6C/EE/79-3

NL

2 of 2
AD
A069209





NATIONAL BUREAU OF STANDARDS

conceptualization of the hardware which might be used in an operational system of this type is included. The results indicate that the numerical ill-conditioning in the problem makes the Extended Kalman Filter a poor choice of estimator. Even after scaling variables and employing a U-D Covariance factorization update algorithm, numerical instabilities in the filter were observed. Recommendations for further work on this topic are included.

Handwritten notes and a vertical arrow pointing upwards.

... digital... processor... not... errors

... digital... processor... not... errors

... digital... processor... not... errors

... digital... processor... not... errors

... digital... processor... not... errors

... digital... processor... not... errors